9
Photolumniscence/Fluorescence Spectroscopic Technique for Nanomaterials Characterizations

9.1
Application of Photoluminescence Spectroscopy in the Characterizations of Nanomaterials

Bingqiang Cao, Haibo Gong, Haibo Zeng, and Weiping Cai

9.1.1
Introduction

Light emission through any process other than blackbody radiation is called *luminescence* and requires external excitation as it is a nonequilibrium process [1]. It is a mechanism through which the excited samples relax to the equilibrium state. In comparison with optical reflection and transmission spectroscopes, luminescence process concentrates on the relaxation of the sample and often provides us more information. For example, impurities of low concentrations in semiconductors are impossible to detect through reflection spectroscopy and more difficult to detect by absorption spectroscopy. However, through luminescence spectroscopy measurements such information could be obtained. Therefore, luminescence spectroscopy is an important and powerful tool to analyze the optical behavior of materials, especially for phosphors and semiconductors. Luminescence processes originate from different excitations that can produce free electrons/holes and their pairs (e–h). Such carriers may recombine across the bandgap or through defect- and impurity-related intermediate levels and emit photons. The excitations can be (i) an intense monochromatic light from a halogen lamp or laser source, (ii) an incident electron beam, (iii) electrical injection of electrons and/or holes through contacts, and (iv) thermal excitation. These emission procedures are known as photoluminescence (PL), cathodoluminescence (CL), electroluminescence (EL), and thermoluminescence (TL), respectively [2]. Electroluminescence is the most difficult to obtain because of the complexity of producing appropriate contacts. However, in terms of the application, EL is the most important since a light emitter has to be able to produce light in an efficient manner under electrical excitation. TL is a technique used with insulators and wide-gap materials and is not widely used. PL and CL are discussed in the following parts in detail with emphases on their applications to characterize the semiconductor nanomaterials.

Nanomaterials: Processing and Characterization with Lasers, First Edition.
Edited by Subhash Chandra Singh, Haibo Zeng, Chunlei Guo, and Weiping Cai.

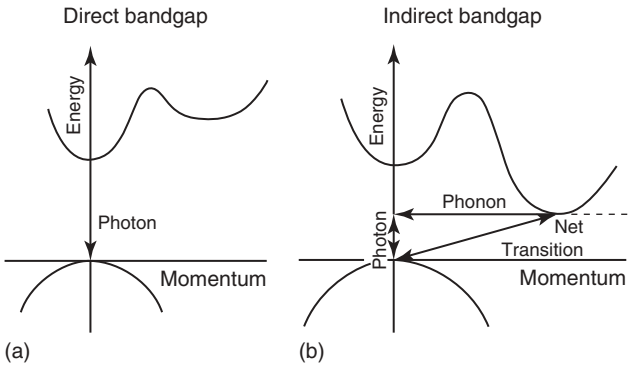

Figure 9.1.1 (a,b) An emission schematic of the differences between a direct bandgap and an indirect bandgap semiconductor with an $E(k)$ diagram.

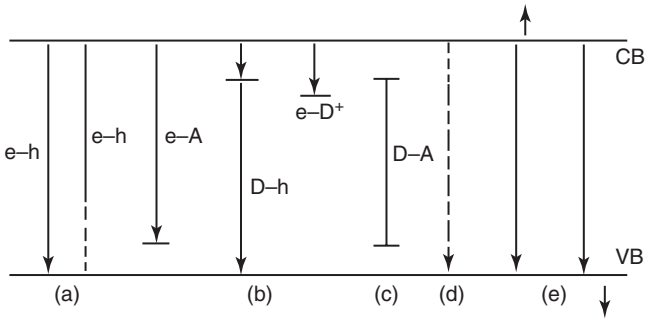

Figure 9.1.2 A schematic of the possible emission process in semiconductors with direct bandgap. (a) Bandgap emission, (b) CB/VB defect recombination, (c) donor–acceptor pair emission, (d) multiphonon emission process, and (e) Auger recombination.

PL is a result of incident photon absorption that generates electron–hole pairs and emits a photon of a different wavelength. The incident photons, when absorbed, excite electrons usually from the valence band into the conduction band through momentum-conserving processes because the photon momentum is negligible. The electrons and holes thermalize to the lowest energy state of their respective bands via phonon emission before recombining across the fundamental bandgap or the defect levels within the bandgap and emitting photons of the corresponding energies. The emitted photon has energy equal to the difference in the energies of states occupied by electrons and holes before recombination, as shown in Figure 9.1.1a. For semiconductors with indirect bandgap as shown in Figure 9.1.1b, the energy relaxation predominantly takes place through phonons, which makes this family of semiconductors inefficient light emitters. For semiconductors with direct bandgap, all possible recombination processes are schematically illustrated in Figure 9.1.2 [3].

PL spectroscopy is an extremely powerful nondestructive technique for assessing material quality [4] including intrinsic electronic transitions between energy bands

and extrinsic electronic transitions at impurities and defects of organic molecules, semiconductors, and insulators. It is quite possibly the most widely used technique when developing a new material system, especially for semiconductors. It is nondestructive and requires virtually no sample preparation or no complex device structures. Moreover, variation of different parameters, for example, temperature, time, or pump power, can be used to obtain band offsets, identify various transitions, and even explore the structural quality of the material. The time evolution of the PL signal can be used to accurately determine the Auger recombination coefficient in other material systems [5].

The study of luminescence from condensed matter is not only of scientific but also of technological interest because it forms the basis of solid-state lasers and it is important for display panels in electronic equipment, lighting, and paints. Moreover, PL frequently provides a nondestructive technique for materials characterization or research in materials.

As a comprehensive survey of PL spectroscopy used on all material systems is beyond the scope of this chapter, only a limited number of topics on PL applications in nanomaterials, in particular, semiconductor nanomaterials are addressed. We first introduce the PL experimental techniques in Section 9.1.2. Then, in Section 9.1.3, we discuss the general PL spectroscopy applications in characterizations of nanomaterial ensembles, for example, room-temperature photoluminescence (RT-PL) and photoluminescence excitation (PLE) spectroscopes, temperature-dependent PL spectroscopy, time-resolved photoluminescence (TRPL) spectroscopy, and excitation-dependent PL spectroscopy. In Section 9.1.4, a special PL spectroscopy, microPL, and its applications in characterizing single nanomaterials are discussed, together with CL, which is also a powerful tool to study the optical properties of single nanomaterials.

9.1.2
Experimental Techniques

A typical and standard PL setup is illustrated in Figure 9.1.3, which is composed of excitation sources, optical elements to focus excitation on the sample and collect the luminescence light, a spectrometer (or filter) to analyze the luminescence, and a detector followed by a data acquisition system. The excitation system usually involves a broad-spectrum source, either a combined tungsten filament for the visible spectrum and deuterium lamp for the UV or a halogen lamp [6]. The lamp emission is passed through a grating monochromator and therefore selectively excites the luminescence. Band-pass or band-edge filters are generally required to eliminate the unwanted second- and higher-order diffraction maxima from the grating. In other cases, to minimize the effect of scattered light, different lasers with their intrinsically narrow linewidths and high intensities, such as He-Cd laser, YAG laser, and semiconductor diode lasers, are chosen as excitation source but suffer from the disadvantage of a fixed wavelength. The sample under investigation is usually fixed in a dark box in a strain-free manner, and sometimes, a cryostat is integrated to provide the desired low temperature near liquid helium or nitrogen.

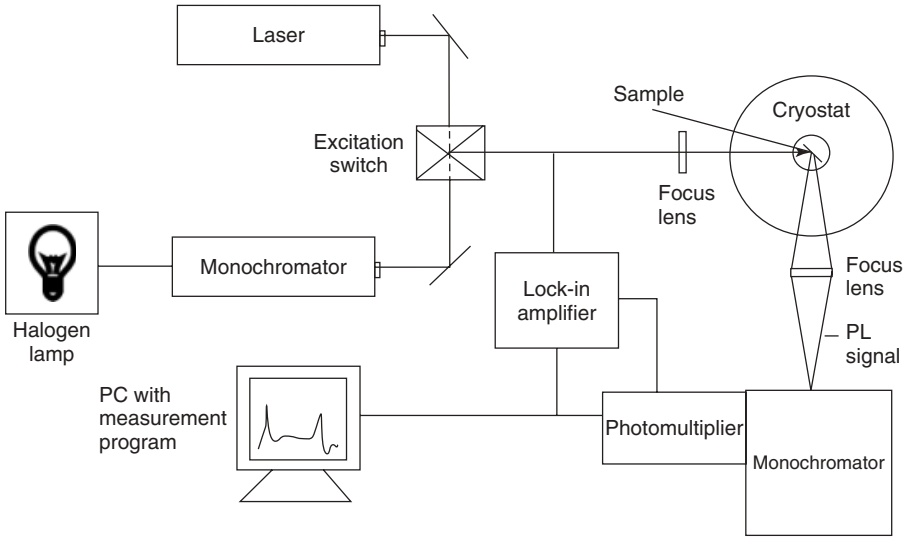

Figure 9.1.3 Schematic view of a generally applied experimental setup for PL spectroscopy measurements with a cryostat station.

Widely used cryostats are closed-cycle refrigerators or cold fingers of helium or nitrogen pipe. As thermally activated nonradiative recombination processes were minimized at low temperature, more spectroscopic information can be obtained from the low-temperature PL spectrum. The luminescence signal is efficiently gathered and focused by optical lens into a second grating monochromator to monitor and analyze the luminescence. The final detector may be a photomultiplier (PMT) or a nitrogen-cooled charge-coupled device (CCD) or photodiode array for improved data collection efficiency at multiple wavelengths. Finally, both the excitation and emission signals were processed with a laptop using some software and a PL spectrum was obtained.

With the similar experimental setup, if the photon energy of the exciting light beam is scanned and, at the same time, some characteristic PL peak intensity is monitored, we can measure the PLE spectrum. PLE may give us some information on the absorption spectrum or on the excited states. In the PLE spectrum, some peaks at positions of stronger absorption can be detected because more electron–hole pairs are created, which means these energies are usually more efficient to excite the monitored PL emission.

TRPL spectroscopy is one of the most powerful tools to investigate the dynamical progress of excited semiconductor samples [6]. To obtain time resolution, one needs a pulsed or temporally modulated excitation source and a time-resolving detection system. Possible excitation sources are modulated continuous-wave lasers, flashlamps, and Q-switched or mode-locked lasers. Till now, two main time-resolving detectors have been developed. One is fluorimeter that uses a fast modulator and phase-sensitive detection to measure the phase shift between luminescence and excitation signals. A time resolution of 50 ps can be measured

in this way. Another is the time-correlated single-photon-counting technique (TCSPT), which can measure decay constants in the picosecond to nanosecond range [7]. TCSPT is based on the detection of single photons of a periodical light signal, the measurement of the detection times of the individual photons and the reconstruction of the waveform from the individual time measurements. In this method, the excitation comes from a fast laser pulse, and the light level reaching the PMT or microchannel plate detector is reduced to such a low level that less than one photon per excitation pulse is detected. The time delay between the photon detection and the time of the pulse is measured, and a histogram of the number of detected photons versus arrival time taken over a large number of excitation pulses is plotted.

9.1.3
Applications of General PL Spectroscopy on Nanomaterial Ensembles

9.1.3.1 Room-Temperature PL and PLE Spectroscopy

The main parameters of interest for RT-PL measurements are the wavelength of emission peak, peak intensity, linewidth, and integrated intensity. The wavelength of the emission peak is of obvious interest for the measured semiconductor sample as it is quite close to the bandgap if the defect-related emissions could be excluded. The other three figures of merit allow for a relative analysis of material quality between samples. Peak intensity is a direct indicator of the semiconductor optical quality. The lower the defect density, the stronger is the peak PL signal if the sample qualities and PL experimental conditions are similar. From the PL linewidth usually measured at half of the maximum, some information about defect density, surface/interface quality, and alloy disorder can be obtained. If the PL peak is typically wide and shows obviously asymmetry, the peaks must be carefully fitted with Gaussian or Lorentzian line shapes [8]. The integrated intensity is somewhat intermediate between the peak intensity and linewidth cases as it depends on both the height and width of the peak. In high-quality samples, the three figures of merit generally track one another.

For PL spectrum measurements of nanomaterials ensembles, it is almost similar to that of bulk or thin-film samples. Figure 9.1.4a shows some ZnO nanoplatelets that are typically tens of nanometers in thickness and several micrometers in dimension on a silicon substrate. Figure 9.1.4b shows the RT-PL spectra of nanosheets that are measured at excitation of the 325 nm He-Cd laser. The full laser exciting power intensity (I_0) is about 2 kW cm^{-2}. A sharp PL peak appears in the ultraviolet region centered at 380 nm with the full width at half maximum (FWHM) of 17 nm, which is near the bandgap of ZnO (3.37 eV at room temperature (RT)). Generally, it is attributed to the bandgap emission or free exciton emission. For direct bandgap semiconductor, the energy $\hbar\varpi$ of excitonic emission can be expressed by $\hbar\varpi = E_g - R^*$, where E_g is the bandgap and R^* is the effective Rydber constant of excitons. For ZnO, the excitonic emission peak is expected at 3.31 eV, which is 60 meV (R^*) lower than the ZnO bandgap of 3.37 eV. However, the emission peak

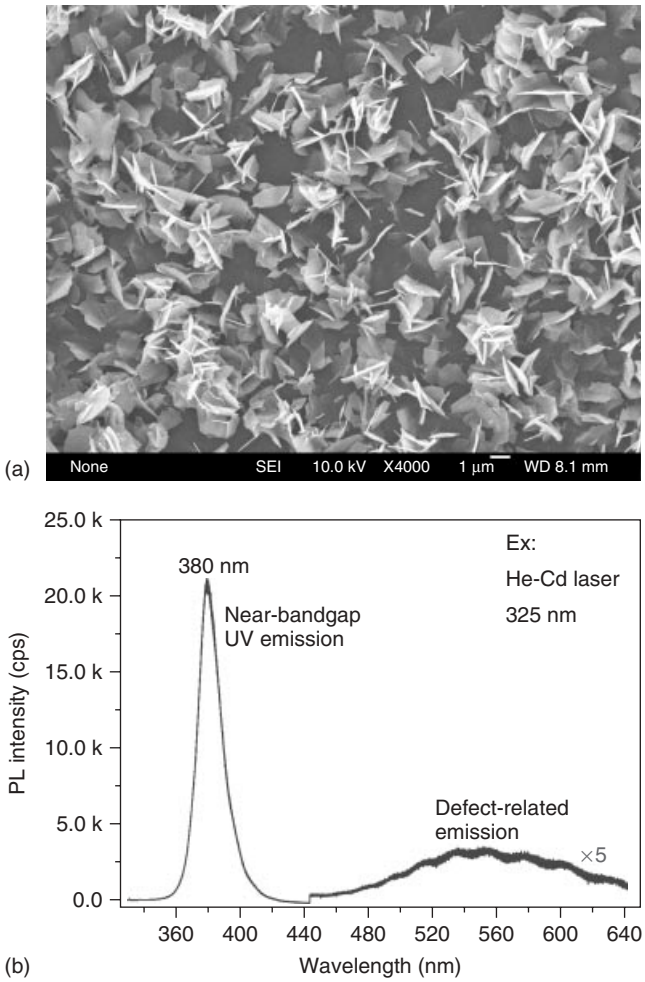

Figure 9.1.4 (a) Scanning electron microscopy image of ZnO nanoplate ensembles on a silicon substrate and (b) the room-temperature PL spectrum of the ZnO nanoplates of (a) excited with a He-Cd laser.

usually shows a slight redshift (40 meV) compared with the theoretical position, which was caused by the heating effect of laser excitation light [9].

At the same time, a rather broad visible emission centered at about 540 nm is also detected. Commonly, this visible emission of ZnO at RT is attributed to the deep-level defects in ZnO crystals, such as oxygen vacancies and/or zinc interstitials. For such ZnO nanoplates, the green emission is much weaker than the UV intrinsic emission. The strong and sharp UV emission in contrast to the weak green emission indicates that the measured ZnO samples are of good crystal quality.

Another powerful way to obtain information about the PL process is the study of the dependence on excitation wavelength of the luminescence spectrum. This is

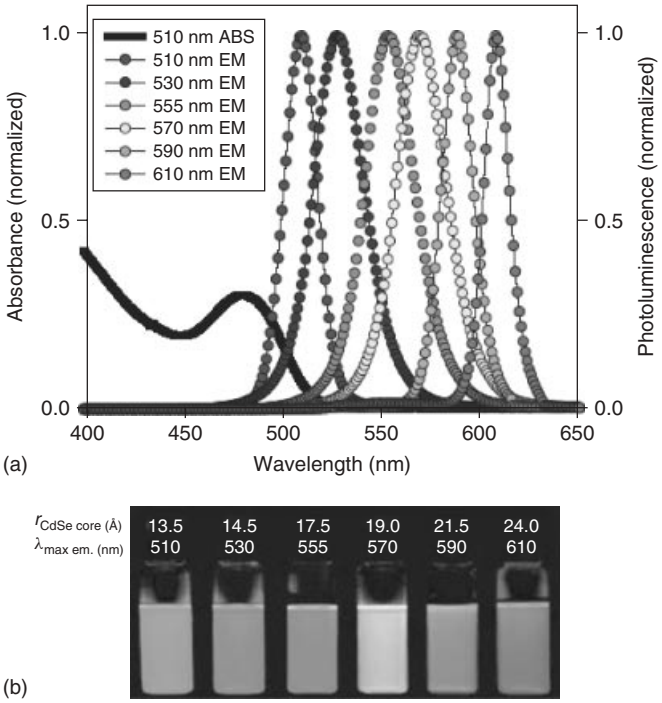

Figure 9.1.5 (a) Absorption and PL spectra of six different CdSe NC dispersions. The black line is the absorption NC of the 510 nm, and others are the PL spectra with different sizes. (b) Photo images the size-tunable luminescence properties and spectral range of the six NC dispersions as correspondingly shown in (a). (Source: From Ref. [10].)

usually performed by recording the PLE spectrum , the excitation wavelength being scanned at fixed luminescence wavelength. Another kind of nanomaterial ensemble typically studied with PL and PLE is semiconductor nanocrystals (NCs) or quantum dots (QDs) [11]. The optical properties of semiconductor NCs are determined by their sizes, shapes, surfaces and bulk defects, impurities, and crystallinity. The luminescence dependence on the NC sizes mainly arises from the quantum size confinement effect, which modifies the density of states near the band edges. When the size of the semiconductor NCs becomes smaller than their Bohr radius, the spatial size confinement of the motion of electrons leads to an increase of their bandgaps. In addition, the actual energy of bandgap absorption becomes sensitive to the size and shape of the NCs. Experimentally, the PL emissions of NCs of different sizes exhibit a series of blueshift toward higher energy from the band edge, as compared to the typical value of the corresponding bulk semiconductors. A typical example of CdSe NCs with different sizes is shown in Figure 9.1.5.

9.1.3.2 **Temperature-Dependent PL Spectroscopy**

In general, sample temperature is an important parameter that influences the PL properties of semiconductors since line narrowing can be expected when

the measured temperature decreases. Moreover, as some nonradiative recombinations can be effectively suppressed when the sample temperature decreases, new ground or excited states can appear at low temperature and a PL spectrum with fine peak structures can be observed. On the other hand, by analyzing the temperature-dependent PL, information about the photodynamics and PL physical origin can be obtained. At present, optical cryostats allow easy operation from room temperature down to a few Kelvins using commercial closed-cycle refrigerators or liquid helium.

Figure 9.1.6 compares the RT-PL and low-temperature (10 K) PL of ZnO nanobelts grown on the silicon substrate with chemical vapor deposition. At room

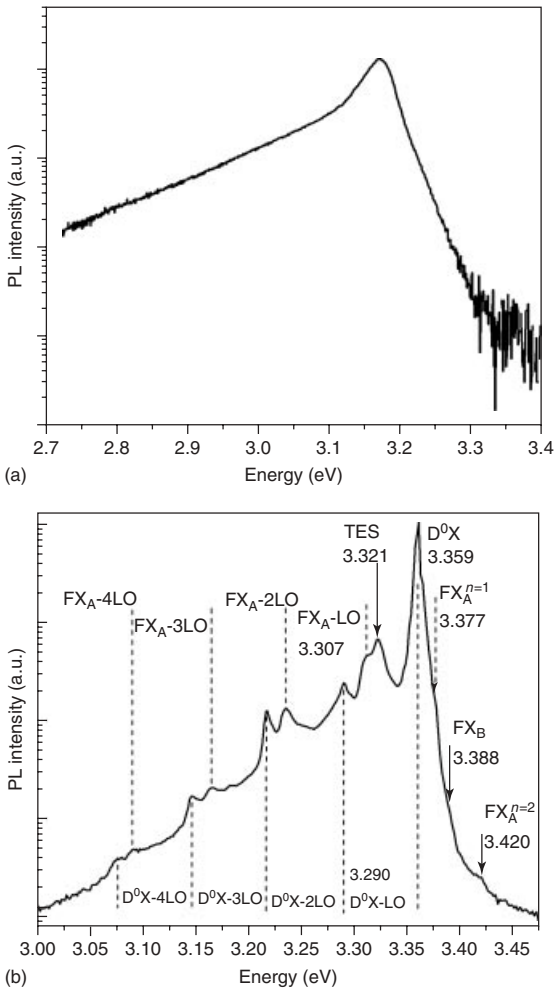

Figure 9.1.6 PL spectra of ZnO nanobelts grown with chemical vapor deposition on silicon substrates (a) measured at room temperature excited with a 355 nm YAG laser and (b) measured at 10 K excited with a He-Cd laser.

temperature, the PL only shows a featureless wide emission peak in the bandgap region. However, the PL spectrum at $T = 10$ K shows more complicated emission peaks. Figure 9.1.6b is dominated by the emission peak at 3.359 eV because of typical donor-bound excitons (D^0X), which is possibly caused by unintentional aluminum dopant. On the high-energy side of this peak, three small shoulders are observed, which can be assigned to the free exciton recombinations as indexed with $FX_{A,B}(n = 1,2)$. Two groups of phonon replica assigned as D^0X-nLO and FX-nLO ($n = 1, 2, 3, 4$) are observed with the energy separation of 72 meV (LO-phonon energy) below the D^0X and FX peaks, respectively. The peak at 3.33 eV is most probably due to a two-electron transition (TET).

The temperature-dependent PL spectra from 10 to 150 K are shown in Figure 9.1.7. It is found that the intensities of the two series of peaks associated with FX and D^0X exhibit an opposite dependence on temperature. The intensities of FX and its related phonon replicas increase with the increasing temperature, while the intensities of D^0X and its replicas decrease and are not detectable at temperature over 70 K. The fast intensity reduction of D^0X is a result of the rapid thermal ionization of bound excitons with increasing temperature. Therefore, more free excitons occupy the ground states. So, from the low-temperature and temperature-dependent PL spectra, the detailed optical characteristics including all kinds of possible recombination process and their dynamics can be well identified.

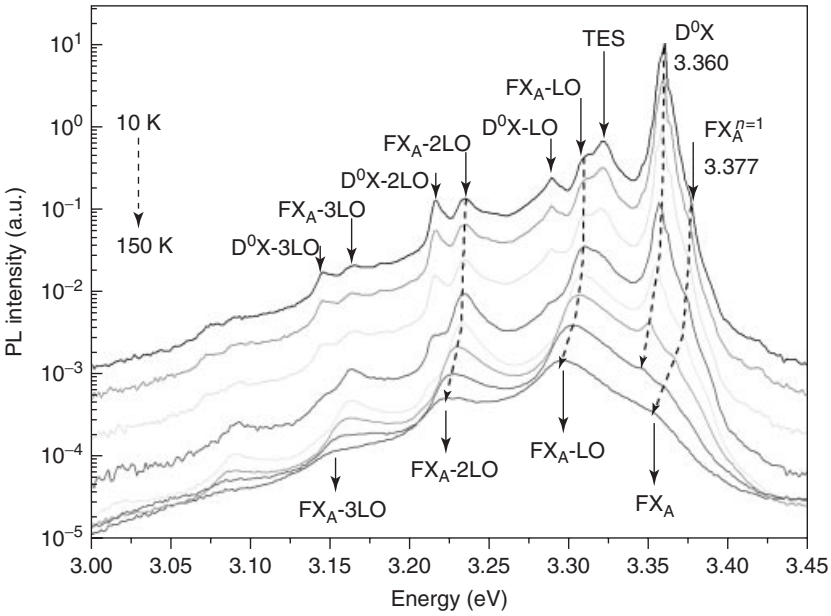

Figure 9.1.7 Temperature-dependent PL spectra of ZnO nanobelts grown with chemical vapor deposition on silicon substrates from 10 to 150 K excited with a He-Cd laser.

9.1.3.3 Time-Resolved PL Spectroscopy

TRPL is another kind of important PL spectroscopy. It is very effective to explore the properties of trapping states. On one hand, the luminescence decay can be detected to compare the lifetime of different trappers to study their emission dynamics. On the other hand, the PL curves can also be collected at a different time after excitation; this helps to directly observe the changes of PL bands. Taking a typical example, Foreman *et al.* [12] measured TRPL of different ZnO samples. Continuous-wave PL spectroscopy was performed by photoexciting the samples with a He-Cd laser operating at 325 nm. The PL was collected and refocused onto an all-silica optical fiber using a complementary pair of aluminum off-axis parabolic mirrors. The collected PL was dispersed by a 30 cm imaging spectrometer and measured using a liquid-nitrogen-cooled CCD camera. However, TRPL spectroscopy was performed by photoexciting the samples with ~100 fs pulses from a 1 kHz, wavelength-tunable optical parametric amplifier tuned to 3.81 eV and by routing the collected PL to a Hamamatsu streak camera with a resolution of 30 ps.

The time-resolved, spectrally integrated band-edge PL of ZnO micropowder, doped micropowder, and nanostructure are presented in Figure 9.1.8. Obviously, the total lifetimes have very large difference. According to the following equations, the decay lines can be fitted by two lifetime components, as listed in Table 9.1.1.

$$I(t) = A_1 e^{-t/\tau_1} + A_2 e^{-t/\tau_2}, \quad A_1 + A_2 = 1$$

The undoped micropowder exhibits the strongest band-edge emission and the weakest defect emission. Although it has the slowest biexponential decay lifetimes, the low quantum efficiency indicates that nonradiative recombination

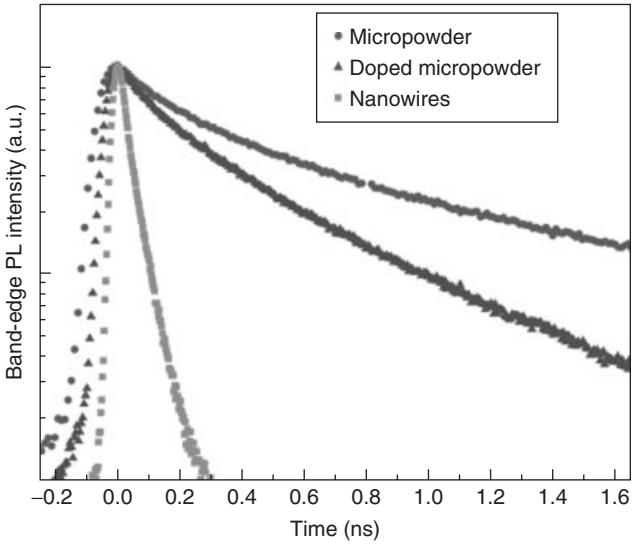

Figure 9.1.8 Time-resolved, spectrally integrated band-edge photoluminescence of ZnO micropowders, sulfur-doped micropowders, and nanostructure. (Source: From Ref. [12].)

Table 9.1.1 TRPL biexponential decay characteristics of band-edge emission for undoped and S-doped ZnO micropowders and nanowires.

	I_D/I_B	UV decay			QE (%)
		τ_1(ns)	τ_2(ns)	A_1	
Undoped powder	0.08	0.198	1.08	0.48	7
ZnO:S powder	320	0.112	0.481	0.37	65
ZnO:S wires	1600	<0.040	–	–	30

Source: From Ref. [12].

dominates band-edge relaxation. Doping the micropowder with sulfur significantly enhances the energy transfer from the band edge to the defect states responsible for visible emission, resulting in reduced band-edge emission, faster band-edge decay, much brighter visible emission, and dramatically increased quantum efficiency. Clearly, the defect-mediated decay channel responsible for visible emission favorably competes with the deleterious nonradiative decay channels. However, when the doped ZnO is formed into nanowires, the band-edge emission decay accelerates beyond the temporal resolution of the instrument and the spectrally integrated quantum efficiency drops. Clearly, nanostructuring increases nonradiative carrier relaxation, thus undermining the channel favorable for visible emission. By TRPL study, it is concluded that as the nanostructure surface-to-volume ratio increases, the nonradiative pathways increasingly competes with the sulfur-induced defects responsible for the bright visible emission.

9.1.3.4 Excitation-Dependent PL Spectroscopy

For the PLE source, excitation energy determined by the wavelength and pumping density determined by the power of excitation source are two important parameters. By changing these two parameters, PL can be measured under different excitation conditions, which are both useful extensions for general PL spectroscopy. For wavelength-dependent PL measurement, a series of wavelengths with insufficient and excessive energies are applied to excite the sample in the normal PL measurement mode. Such PL results can be used to study the correlation between the excited states and emission energy and hence help to explore the luminescence transition mechanisms and can also be very effective to explore the characters of defect levels located in the bandgap.

The following is an example of our recent results about defect-related PL of ZnO nanoparticles (NPs) by wavelength-dependent PL measurement. The selected ZnO NPs have an average diameter of 20 nm and were synthesized by laser ablation in liquid [14]. Strong blue emissions can be obtained from these ZnO NPs, but the mechanism of this kind of defect-related PL is still unclear. Figure 9.1.9 presents the excitation-dependent PL spectra of such ZnO NPs. The blue PL intensities exhibit

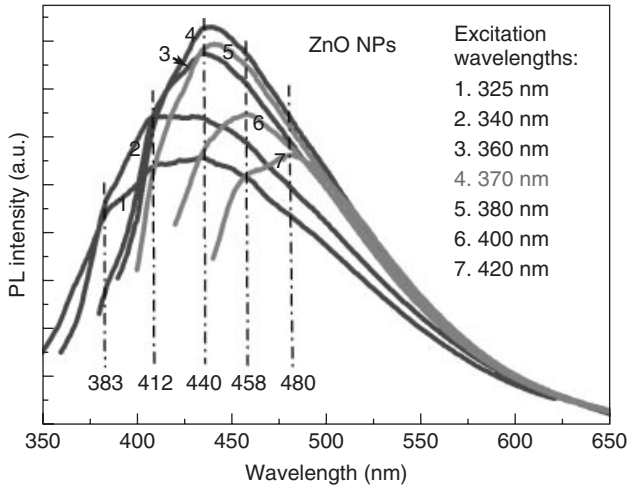

Figure 9.1.9 Time-resolved excitation wavelength-dependent photoluminescence of ZnO nanoparticles. (Source: From Ref. [13].)

nonlinear increase–decrease dependence on excitation – first they increase, then reach saturation under bandgap energy (E_g) excitation, and then decrease, but still effectively emit with excitation energy (E_{ex}) smaller than E_g. Among these universal excitation-dependent features, the most important is that $E_{ex} = E_g$ energy is the optimal excitation and $E_{ex} < E_g$ energy can still effectively excite blue emissions.

The fact that blue emissions can be effectively excited by $E_{ex} < E_g$ energy demonstrates that the excited states and initial states of corresponding transitions could be located below the conduction band edge, not at or above the conduction band edge. Under $E_{ex} = E_g$ excitation, the electrons can be first be excited up to conduction band, then nonradiatively transit into above initial states, and then radiatively transit and emit blue emissions. The fixed emitting wavelengths indicate several different energy gaps from initial states to end states, such as 3.0 eV (412 nm), 2.8 eV (440 nm), and 2.7 eV (458 nm). Combining such excitation-dependent PL spectra and other analyses such as reported defect levels and formation energy, the observed initial state was suggested to be correlated with Zn interstitials, and there could be several derivative levels with lower energy involved in possible localization or coupling with other defects.

With the development of high-power laser, the excitation density can be tuned to as high as gigawatts per square centimeters. Under high excitation, the optical properties of materials will show some different characters, which are called *nonlinear optics*. This is a totally different research topic in optics and is not discussed in this chapter. However, it should be noted that some groups have found that under excitation density of few kilowatts per square centimeters or megawatts per square centimeters, nanomaterials show some nonlinear optic properties, such as random lasers [15] and nanowire lasers [16].

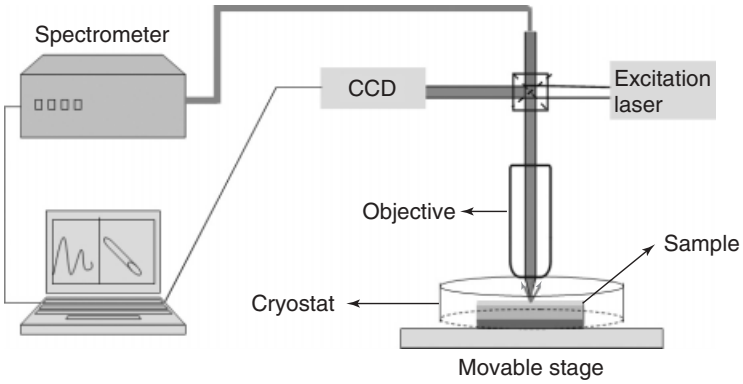

Figure 9.1.10 Schematic view of a typical microPL experimental setup.

9.1.4 Applications of MicroPL Spectroscopy on Single Nanomaterial

9.1.4.1 MicroPL Spectroscopy and Its Applications on Single Nanomaterial

The main difficulty of the PL measurements on single nanomaterials lies in focusing excitation laser on single nanomaterials at the nanoscale. At the same time, the emission signal is rather weak. To overcome these difficulties, microPL is usually built with an optical microscope to focus and detect the excitation and emission light, respectively, as shown in Figure 9.1.10. Moreover, a CCD is also integrated for sample imaging. For typical microPL, its spatial resolution is about 1 μm. Therefore, microPL is very useful to characterize single nanomaterials, such as single semiconductor nanowires [17], carbon nanotubes [18], and graphene [19]. The applications of microPL in single nanomaterials including PL, PLE, TRPL, and temperature-dependent PL are similar to those of general PL spectroscopy.

Figure 9.1.11a shows a far-field image of a single GaN nanowire, which was back illuminated with a lamp. The localization of bright emission at the ends of the wire suggests strong wave-guiding behavior of the Fabry–Perot nanowire laser [20]. Figure 9.1.11b shows the microPL spectrum of the single GaN nanowire. The broad and weak spectrum was excited with a 1 mW continuous-wave excitation (He-Cd laser).However, when the sample was excited with a 1 $\mu J\,cm^{-2}$ pulsed excitation using Ti: sapphire laser and optical parametric amplifier, several sharp (<1.0 nm) features appeared in the spectrum, indicating the onset of stimulated emission, which is consistent with observed laser actions in Figure 9.1.11a.

9.1.4.2 CL Spectroscopy

CL refers to luminescence from a sample excited by an electron beam, which is usually measured by means of the system based on a scanning electron microscope (SEM) [21]. The electron beam is emitted from an electron gun of the SEM, collected by electron lenses, and then focused on a sample. The luminescence

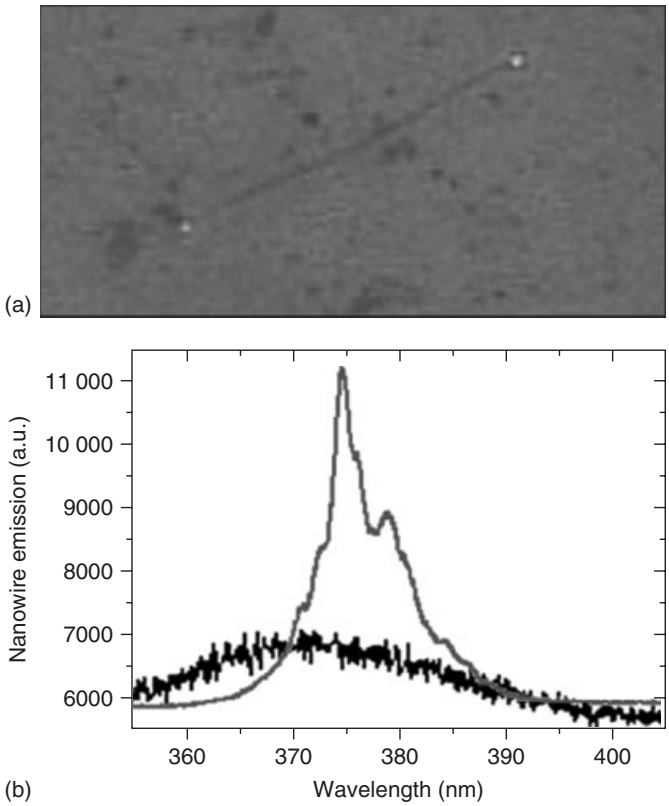

Figure 9.1.11 (a) Far-field image of a single GaN nanolaser and (b) microPL spectrum of the single GaN nanowire. (Source: From Ref. [20].)

from the excited sample is collected by an ellipsoidal mirror and then sent to a spectrometer equipped with a CCD camera, as schematically shown in Figure 9.1.12. Using SEM for sample location, CL usually has a lateral resolution better than 10 nm as the de Broglie wavelength of electrons is much shorter than light wavelengths. On the other hand, the SEM electron beam can be focused on a spot size of tens of nanometers and scanned over the area of the sample. By CL intensity mapping, one can obtain not only spectroscopic information but also spatial details. Therefore, CL is very appropriate for characterizations of single nanostructure because of its high resolution and intensity scanning beyond the optical diffraction limit.

9.1.4.3 Applications of CL in Single Nanomaterials

Figure 9.1.13a,b shows the proposed structure of ZnO/ZnMgO quantum well (QW) nanowire grown with a two-step pulsed laser deposition (PLD) and its corresponding SEM image. Clearly, it is almost impossible to measure such single

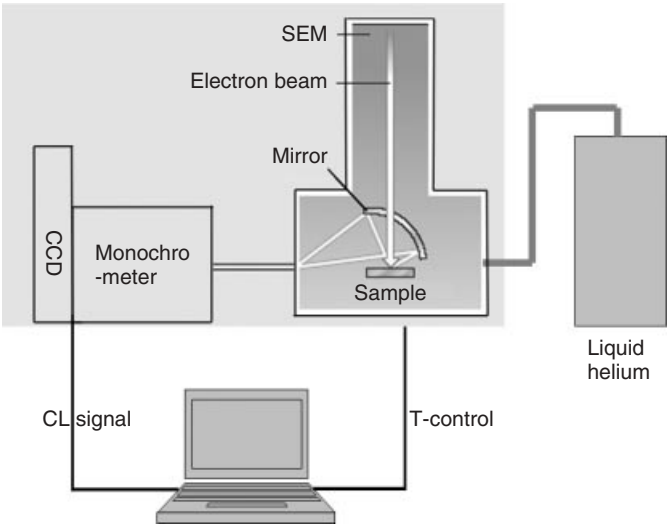

Figure 9.1.12 Schematic view of a generally applied experimental setup for the CL spectroscopy measurements with a cryostat station equipped on a scanning electrony microscope.

nanowires with traditional PL. For microPL, it is also difficult as, with optical microscopy, the single nanowire cannot be well focused. In this case, CL would be a very powerful tool to access the quality and uniformity of such core–shell nanowire heterostructure. To focus the CL measurement on a single nanowire, the sample is 60° tiled in the SEM chamber. So, by focusing the excitation electron beam on a single nanowire, CL spectrum can be detected from the different parts of a single nanowire, as shown in Figure 9.1.13c. In addition to the emissions from the ZnO core at 3.36 eV and ZnMgO barrier at 3.52 eV, another new peak at 3.45 eV is detected from the different parts of the wire. These emissions are caused by the exciton recombination confined in the radial nanowire QW. At the same time, a film QW with bigger thickness is also detected from the substrate.

Spatially resolved CL intensity mapping is another useful method to study the carrier distribution in the QW nanowire. Figure 9.1.14a,b shows the SEM image and a typical CL spectrum of the scanned QW nanowire. Figure 9.1.14c is the CL intensity map monitored at different peak energies of ZnO, QW, and ZnMgO barrier. The intensity map of the ZnO core is very homogeneous, which reflects the high-quality crystal of the core nanowire and homogeneous distribution of excitons. The intensity map of the QW distributes along the whole nanowire from the tip to the bottom. Moreover, the QW intensity of the tip part is a little stronger. It means that both the radial QW around the side face and axial QW on the tip of the nanowire are grown. However, the ZnMgO barrier CL intensity of the wire stem is much weaker than that of the tip part. The radial ZnMgO does not show up because the carriers are quickly captured into the radial QW and recombine radiatively. By high-resolution special and spectral CL, the relation

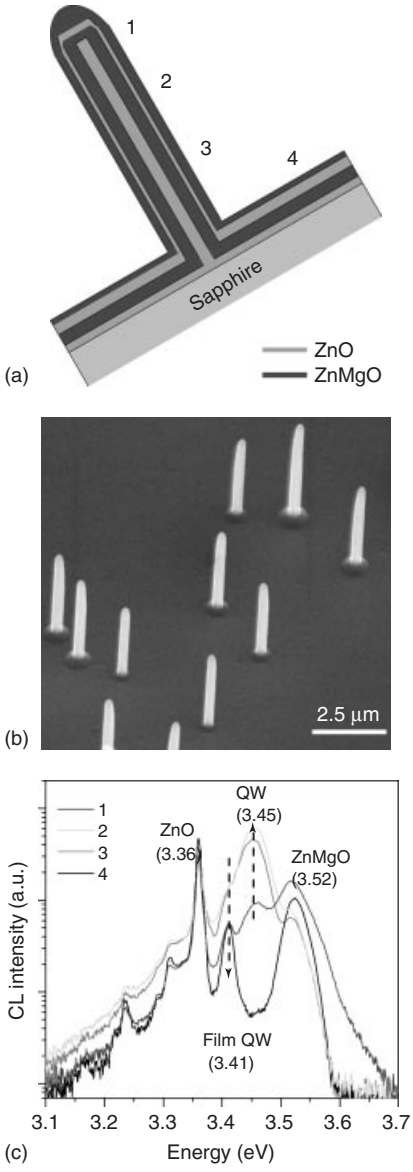

Figure 9.1.13 (a) Schematic structure of the proposed ZnO/ZnMgO quantum well nanowire, (b) SEM image of the low-density ZnO quantum well nanowire, and (c) CL spectrum measured from a single quantum well nanowire at $T = 10$ K. (Source: From Ref. [22].)

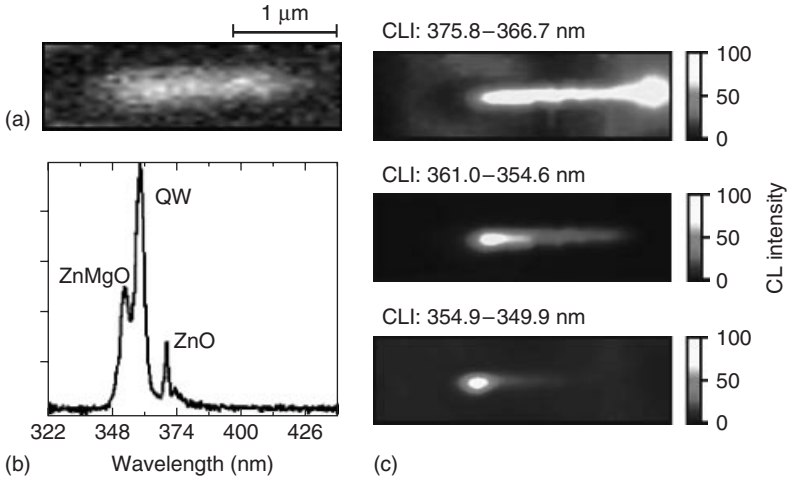

Figure 9.1.14 (a) An SEM image and (b) a typical CL spectrum measured from a single ZnO QW (15 pulses) nanowire; the ablated laser pulses for QW growth are 15; and (c) CL intensity maps of a single ZnO/ZnMgO QW nanowire. From top to bottom, the intensity maps correspond to the CL of ZnO, QW, and ZnMgO, respectively.

between the detailed optical properties and its structure characters can be clearly demonstrated.

9.1.5 Conclusions

As a traditional optical characterization technique, PL spectroscopy continues to be a powerful tool for the investigation of optical properties of nanomaterials. In this review chapter, not only experimental equipments but also information that properties or material parameters can be obtained with respective techniques are summarized. The foregoing examples demonstrate well the breadth of novel experiments that can be performed with different kinds of PL methods. We still believe that, because of their scientific and technological interests, the study of luminescence properties of materials, including nanomaterials, will show new developments and findings in the future. More additional reference can be find in Ref. [23].

Acknowledgments

This work is supported by NSFC (51002065, 11174112) and Shandong provincial science foundation (BS2010CL003). BC thanks the Taishan Scholar Professorship (TSHW20091007) tenured at the University of Jinan. The Program for New Century Excellent Talents in University and the Research Foundation for Returned Overseas Students, Ministry of Education, China, are also acknowledged.

References

1. Morkoç, H. and Özgür, Ü. (2009) *Zinc Oxide: Fundamental, Materials and Device Technologies*, John Wiley & Sons, Inc.
2. Czichos, H., Saito, T., and Smith, L. (eds) (2006) *Handbook of Materials Measurement and Methods*, Springer.
3. Klingshirn, C. (2001) *Semiconductor Optics*, Springer.
4. Willardson, R.K. and Beer, A.C. (eds) (1972) *Semiconductors and Semimetals*, Academic Press.
5. Henimi, M. (2005) *Dilute Nitride Semiconductor*, Elsevier.
6. Kasap, S. and Capper, P. (eds) (2006) *Handbook of Electronic and Photonic Materials*, Springer.
7. Becker, W. (2005) *Advanced Time-Correlated Single Photon Counting Techniques*, Springer.
8. Cao, B.Q., Cai, W.P., and Zeng, H.B. (2006) *Appl. Phys. Lett.*, **88**, 161101.
9. Cao, B.Q., Cai, W.P., Li, Y., Sun, F.Q., and Zhang, L.D. (2005) *Nanotechnology*, **16**, 1734.
10. Medintz, I.L., Uyeda, H.T., Goldman, E.R., and Mattoussi, H. (2005) *Nat. Mater.*, **4**, 435.
11. Wiederrecht, G.P. (ed.) (2010) *Handbook of Nanoscale Optics and Electronics*, Elsevier.
12. Foreman, J.V., Li, J., Peng, H.Y., Choi, S., Everitt, H.O., and Liu, J. (2006) *Nano. Lett.*, **6**, 1126.
13. Zeng, H.B., Yang, S.K., Xu, X.X., and Cai, W.P. (2009) *Appl. Phys. Lett.*, **95**, 191904.
14. Zeng, H.B., Cai, W.P., Li, Y., Hu, J.L., and Liu, P.S. (2005) *J. Phys. Chem. B*, **109**, 18260.
15. Cao, H., Xu, J.Y., Zhang, D.Z., Chang, S.H., Ho, S.T., Seelig, E.W., Liu, X., and Chang, R.P.H. (2000) *Phys. Rev. Lett.*, **84**, 5584.
16. Gargas, D.J., Toimil-Molares, M.E., and Yang, P.D. (2009) *J. Am. Chem. Soc.*, **131**, 2125.
17. Czekalla, C., Sturm, C., Schmidt-Grund, R., Cao, B.Q., Lorenz, M., and Grundmann, M. (2008) *Appl. Phys. Lett.*, **92**, 241102.
18. Lefebvre, J., Fraser, J.M., Finnie, P., and Homma, Y. (2004) *Phys. Rev. B*, **69**, 075403.
19. Gokus, T., Nair, R.R., Bonetti, A., Böhmler, M., Lombardo, A., Novoselov, K.S., Geim, A.K., Ferrari, A.C., and Hartschuh, A. (2009) *ACS Nano*, **3**, 3963.
20. Johnson, J.C., Choi, H.J., Knutsen, K.P., Schaller, R.D., Yang, P.D., and Saykally, R.J. (2005) *Nat. Mater.*, **1**, 106.
21. Czichos, H., Saito, T., and Smith, L. (eds) (2006) *Springer Handbook of Materials Measurement Methods*, Springer.
22. Cao, B.Q., Zúñiga-Pérez, J., Boukos, N., Czekalla, C., Hilmer, H., Lenzner, J., Travlos, A., Lorenz, M., and Grundmann, M. (2009) *Nanotechnology*, **20**, 305701.
23. Additional reference (a) Singh, J. (ed.) (2006) *Optical Properties of Condensed Matter and Applications*, John Wiley & Sons, Inc.; (b) Toyozawa, Y. (2003) *Optical Process in Solids*, Cambridge University Press; (c) Fox, M. (2001) *Optical Properties of Solids*, Oxford University Press; (d) Demtröder, W. (2002) *Laser Spectroscopy*, Springer.

9.2
Fluorescence Correlation Spectroscopy of Nanomaterials

Kaushal Kumar, Luigi Sanguigno, Filippo Causa, and Paolo Antonio Netti

9.2.1
Introduction

Nanotechnology refers to the research and technology developments of atomic and molecular entities at nanometer length scale. From the past two decades, the research on nanomaterials has grown explosively, and nowadays, it has become a matter of much debate because of its huge potential in future technological advancements [1, 2]. Nanotechnology may be able to create many new materials and devices with a vast range of applications, such as in medicine, electronics, biomaterials, energy production, and in other fields where materials are being used. A decade ago, nanoparticles were studied because of their size-dependent physical and chemical properties, but now they have entered into the commercial exploration age for use in our medicines, cosmetic products, biomedical diagnosis, and so on. Nanoscale structures and materials (e.g., nanoparticles, nanowires, nanofibers, and nanotubes) have been vastly explored in biological applications such as biosensing, biological separation, molecular imaging, and anticancer therapy because of their novel properties and new functions that differ from their bulk counterparts [3–5]. Particularly, their high volume/surface ratio, surface tailorability, improved solubility, and multifunctionality open many new possibilities for biomedicine [3]. Moreover, nanomaterials offer remarkable opportunities to study and regulate the complex biological processes for biomedical applications in an unprecedented manner, and intense research is going on in this direction. The typical cell size of living organisms is $\sim$10 μm, and it contains submicrometer-sized components. These submicrometer-sized components can easily be probed by the use of the nanoparticles and allow us to detect cellular machinery without introducing too much interference [6]. Understanding biological processes at the nanoscale level is a strong driving force behind the development of nanotechnology in biological areas [6].

The popularity of word ''nano'' is not too old, although there are some evidences of nanomaterials in the past [7]. Earlier studies on nanosized materials concentrated on the synthesis nanoparticles in order to produce size- and shape-controlled particles of various materials. But now, we have wise synthesis routes, and only efforts are needed to apply nanoparticles into practical devices. As mentioned above, several products based on nanomaterials are now available commercially, but the research does not end here. As society has begun using consumer products based on nanomaterials in greater quantities, the interest in the broader implications of these products has also grown. A number of serious concerns have been raised about what effects these will have on our society and what action, if any, is appropriate to mitigate these risks. The central question is whether the unknown risks of engineered nanoparticles can spoil the established benefits. At present, it

Nanomaterials: Processing and Characterization with Lasers, First Edition.
Edited by Subhash Chandra Singh, Haibo Zeng, Chunlei Guo, and Weiping Cai.

is proved that nanomaterials can be a health hazard for humans [8, 9], and it opens a new field of research, *nanotoxicology* [10, 11]. Recent study shows that inhaled ultrafine particles exert respiratory effects; they translocate from the lung into the circulatory system [8, 12] and result in cardiovascular problems. In future, this issue will be more prominent and major funding would be needed to research on health and environment friendly products. Because of its vast capability in improving device efficiency, research will go ahead on both positive and negative impacts of nanotechnology. At present, there are numerous applications of various types of nanomaterials inside cells ranging from cell imaging and cell tracking to cancer treatment. Here we mention some examples of biomedical applications where nanoparticles are in use.

- Fluorescent biological labels [13]
- Drug and gene delivery [14]
- Biodetection of pathogens [15]
- Detection of proteins [16]
- Probing of DNA structure [17]
- Tissue engineering [18]
- Tumor destruction via heating (hyperthermia) [19]
- MRI contrast enhancement [20].

Detailed description of the above said applications can be found in respective references. The possibility of using nanoparticles as superior labels and sensors in biological studies has sparked widespread interest. In the above-mentioned examples, the nanoparticles come closer to the cell and interaction between the cell components and nanoparticles gives rise to specific signals, which are detected by external devices. In order to apply nanoparticles in these areas, it is necessary to understand diffusion and localization of nanoparticles in the cells. The uptake and cellular location of nanoparticles is a field of major interest in the context of drug delivery [21]. Metal nanoparticles have also found increasing application in live cell imaging [22].

In order to probe the biomolecular interactions, scientists rely on a group of techniques. Since the biological process occurs in a dilute medium, it is highly essential to investigate these processes at the single-molecule level where single/few nanoparticles interact with target. Conventional ensemble techniques used for investigating biomolecular interactions such as mass spectrometry, X-ray crystallography, NMR, and so on provide information on bulk samples and in nonphysiological conditions. These techniques do not have the capability to detect the molecules at single-molecule level. But the advancement of science and technology in recent decades has led to the emergence of biophysical techniques that are capable of probing single molecules in very dilute solutions in real time. By focusing on an individual molecule in space and time, such analyses provide quantitative information about force properties, conformational dynamics, molecular interactions, and temporal changes with its microenvironment that could otherwise be hidden in ensemble experiments. Molecular dynamics can be studied without having to bring the ensemble population into a nonequilibrium state. Furthermore, because of the use of smaller sample volume, the high spatial

resolution of single-molecule techniques provides the opportunity to look at rare molecular events that exist only in highly localized regions of the cell.

One approach to single-molecule detection is the optical method based on fluorescence detection. Fluorescence techniques are noninvasive and nondestructive to biological samples. They can be performed in real time at ambient or physiological temperatures. Their versatility with the molecular environment implies that they may be applied *in vitro* or *in vivo*. Since in very dilute systems, fluorescence emission intensity becomes very low, systems based on the measurement of emitted intensity become appropriate. In subnanomolar concentrations, another group of fluorescence methods that monitor the fluorescence intensity fluctuations of single molecules moving in and out of a confined illuminated volume have been developed [23, 24]. This method is known as fluorescence fluctuation spectroscopy (FFS), which provides information that lies hidden in the fluctuating signal such as dynamic processes, chemical kinetics, or molecular interactions. One of the first FFS method was introduced by Magde, Elson, and Webb in 1972 [25] and is known as fluorescence correlation spectroscopy (FCS). It uses intensity fluctuations of fluorescent particles diffusing through a focused laser beam, to characterize translational diffusion coefficients and chemical rate constants. The improvement of this technique for single-molecule sensitivity was achieved by using a confocal microscope with a high numerical aperture (NA) objective and single-photon counting avalanche photodiodes (APDs) as detectors. Since then, it has become an increasingly popular technique for the study of dynamics in physiological environment at thermodynamic equilibrium. The technique was originally developed to study the bimolecular interactions at physiological regime, but now this technique is also used to study the dynamics of inorganic fluorescent nanomaterials and has vast potential to characterize nanomaterials.

Besides this, another variant of this technique emerged recently and is based on the detection of the dark part of the emitted energy from excited molecule. The FCS technique needs that particles/molecules under probe have good fluorescence quantum yield. Many particles and molecules do not show good fluorescence emission (bright part) property; rather a major part of the excitation goes through nonradiative way (dark part). Thus, nonfluorescent particles/molecules need to be tagged with other fluorescent molecules to make FCS measurement possible. This is the limitation of FCS for nonideal fluorophores. The new variant known as photothermal correlation spectroscopy (PhCS) is suitable for nonfluorescent molecules and eliminates the necessity of molecular tagging [26, 27]. Particularly, it is suitable for absorbing semiconducting and metallic nanoparticles [27]. Analogous to FCS, it measures the time correlation function of the particle's photothermal signal, which is directly proportional to the light absorption by the particle and is thus named PhCS. Since absorption by metal nanoparticles neither saturates nor photobleaches at reasonable excitation intensities or has complicated photophysics, PhCS is free from the limitation encountered by FCS.

In this chapter, the authors intend to make familiar readers with this technique who want to study the dynamical behavior of nanoparticles in solution and

nanoparticle–cell interaction. The chapter would also provide guidelines to the readers in establishing own homebuilt FCS setup.

9.2.1.1 What FCS Can Do for Nanoparticles?

FCS can perform two tasks: first, testing the stability of single or multicomponent nanoparticles in a liquid medium, and second, finding out interaction mechanisms of nanoparticles with others such as cellular molecules. The first criterion for the applicability of nanoparticles is that they should be stable for a specific time period. For cellular and many other applications, the formation of stable solutions of nanoparticles in buffer media is important, and not all the nanoparticles have been found to be stable as hydrosols in solutions. The stability of hydrosols strongly depends on the surface potential of the particles, the zeta potential, pH, and salt concentration of the solvent. FCS can reveal the stability of nanoparticles in an aqueous medium and has now become a common tool for characterizing the properties of nanoparticles in solution [28]. This technique is particularly useful in the characterization of fluorescent nanoparticles because FCS is based on fluorescence emission. FCS can measure the concentration, brightness, hydrodynamic radius, and monodispersity of the fluorescent probe in a single measurement, allowing for rapid characterization of probes in solution [29]. Cellular interaction with nanoparticles depends on various physical properties of nanoparticles such as size, shape, surface charge density, surface chemistry, and degree of aggregation, and understanding how these properties influence the interaction mechanism will lead to a predictive model for nanoparticle–cell interaction. Any phenomenon that alters the motion of nanoparticles could be probed using FCS technique.

9.2.1.2 Fluorescence Is a Tool for FCS

A typical fluorescent molecule emits 10^5 photons before photobleaching in water and at rates up to $10^9\ s^{-1}$ (at least during microsecond bursts before ground state depletion by intersystem crossing to excited triplet states). Modern photon detectors, laser excitation, and high NA microscopy optics allow collection of 3% of the emitted fluorescence photons. Sometimes, 100 photons can be detected when a single molecule in solution is diffusing (in less than a millisecond) through the focus of a laser beam tuned to excite the target fluorophore. So recognition and identification of the individual target molecule above the background fluorescence of the buffer can be easily done in appropriate liquid solvents. The photon detection rate from individual molecules is used by FCS for the determination of fundamental dynamical parameters. Measurement scales from microseconds to seconds are easily accessible and cover transport coefficients, chemical kinetics, and recognition of aggregation in samples.

9.2.1.3 How Does FCS Work?

In an FCS experiment, the fluorescence emitted from a small, optically well-defined open-volume element of a solution in equilibrium is monitored as a function of time (Figure 9.2.1a). The recorded fluorescence emission signal is proportional to the number of fluorescent molecules in the probe volume. This number fluctuates

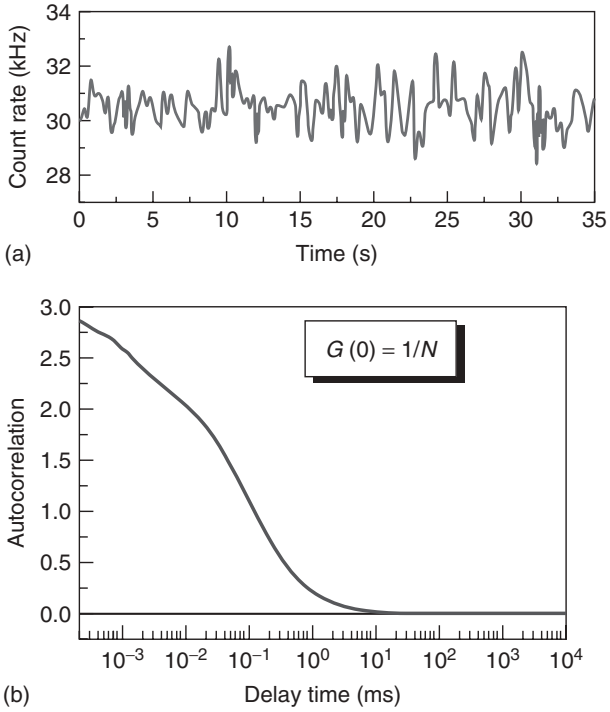

Figure 9.2.1 (a) The fluorescence signal (raw data) recorded from the volume fluctuates in time. (b) A temporal autocorrelation of this fluctuating signal exhibits characteristic decay times corresponding to the relaxation times for chemical kinetics and diffusion.

about its equilibrium value as molecules diffuse in and out of the volume. The temporal autocorrelation of the fluorescence signal fluctuation (Figure 9.2.1b) yields the timescale of such dynamics, and its variance yields the average number of independent fluorophores (N) in the probe volume. The correlation functions contain information about chemical reaction kinetics, coefficients of diffusion, and equilibrium chemical concentrations. Mathematically, the normalized autocorrelation function $G(T)$ is calculated as the time average of the product of the fluctuations in detected fluorescence at every time t and the fluctuations at delayed times $t + \mathrm{d}T$, normalized by the squared time average of the fluorescence emission.

9.2.1.4 **Basic Theory of FCS**

Ideally, FCS works in very dilute samples, in average, one particle per excitation volume, and measures fluorescence intensity fluctuation. In a typical FCS setup, a laser beam is focused on a solution under thermal equilibrium. The focused laser beam, wavelength, and detection optics define the probe volume of the system. The pinhole spatially filters the emitted fluorescent light to ensure that only light from the focus is detected. The concept of confocal arrangement can

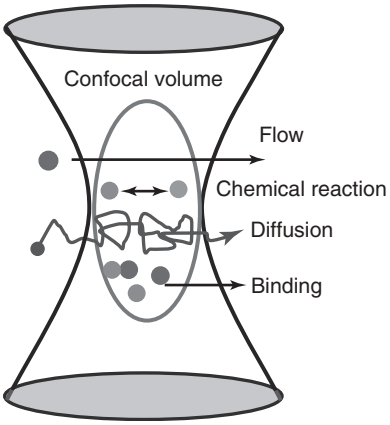

Figure 9.2.2 Fluorescent solute molecules (circles) fluctuate in a small elliptical volume about an average value as molecules diffuse in and out of the volume. Figure shows various dynamical processes that FCS can measure.

be found in Ref. [28]. A typical FCS setup measures various dynamical processes as depicted in Figure 9.2.2. As fluorescent particles move in and out of this minute region, the total fluorescence $F(t)$ detected will fluctuate in time due to the change in the total number of molecules, $N(t)$, present in the probe volume. The time-dependent autocorrelation function of $F(t)$ contains information about the average duration and amplitude of the fluctuations. The decay rate and the shape of the autocorrelation function, $G(\tau)$, give the mechanism of the process and the residence time of the particles inside the probe volume. The magnitude of $G(\tau)$ provides information about the number density of the fluorescent molecules or particles in the probe volume. The total detected fluorescence $F(t)$ is proportional to the number of particles in the focal volume, $N(t)$. The normalized autocorrelation function is defined as

$$G(\tau) = \frac{\langle \delta F(t+\tau)\delta F(t)\rangle}{\langle F(t)\rangle^2} \tag{9.2.1}$$

where $\delta F(t) = F(t) - \langle F(t)\rangle$ is the fluctuation of the fluorescence signal $F(t)$ at about its average value and $\langle\ \rangle$ denotes an ensemble average. The fluctuation correlation function requires the calculation of the intensity time average before calculating the correlation functions. δF can be defined as

$$\delta F(t) = KQ \int_{\text{all space}} \delta C(r,t) I(r) \phi(r) \mathrm{d}r \tag{9.2.2}$$

where $\delta C(r,t)$ is the concentration fluctuation, $I(r)$ is the excitation intensity profile, $\phi(r)$ is the collection efficiency function that characterizes the spatial filtering effect of the pinhole on the point spread function (PSF), K is the detection efficiency of the instrument, and Q is the product of the absorption coefficient and the molecular quantum yield of the particle. The PSF of the optical design describes the intensity distribution of the image of a point emitter [30, 31].

The product of $I(r)$ and $\phi(r)$ gives the molecule detection function (MDF) (r) that determines the spatial distribution of the effective sample volume. The MDF depends on the intensity distribution of the focused laser illumination and the efficiency of photons detected from a fluorescent molecule. The factors K and Q can be combined to fluorescence yield parameter, η that is determined by the photon counts per molecule per second.

In diffraction-limited illumination and detection scheme, the PSF is described by Bessel function, while for an underfilled back aperture of objective illumination, it is approximated as a Gaussian–Gaussian–Lorentzian (x, y, z) intensity profile. The PSF of a microscope objective is then convoluted with the circular pinhole function to give MDF (r) and then approximated as 3D Gaussian illumination intensity profile

$$\mathrm{MDF}(r) = I_0 \mathrm{e}^{-2r^2/r_0^2} \mathrm{e}^{-z^2/z_0^2} \tag{9.2.3}$$

where $I_0 = 2P/(\pi r_0^2)$ is the excitation intensity at the center of the laser beam waist with laser power, P; z is the distance along the axial direction from the focal plane, and z_0 is the intensity dropped to $1/e^2$; r_0 is the diffraction-limited beam waist radius at $z = 0$ and is given by

$$r_0 = \frac{0.61\lambda}{\mathrm{NA}} \tag{9.2.4}$$

where NA is the numerical aperture of the microscope objective and λ is the excitation wavelength. Equation (9.2.3) along with Eq. (9.2.4) gives effective excitation volume as

$$V_{\mathrm{eff}} = \pi^{3/2} r_0^2 z_0 \tag{9.2.5}$$

Using Eqs. (9.2.1–9.2.5) and at $\tau = 0$, the correlation function can be expressed as

$$G(0) = \frac{\langle \delta F(t) \rangle^2}{\langle F(t) \rangle^2} = \frac{1}{V_{\mathrm{eff}} \langle C \rangle} = \frac{1}{\langle N \rangle} \tag{9.2.6}$$

Thus, inverse of $G(0)$ gives the absolute number of particles in the probe volume. In Eq. (9.2.6), it is taken that the number of photons fluctuates according to Poisson statistics, $\langle \delta N^2 \rangle = \langle N \rangle$.

The concentration fluctuation, $\delta C(r, t)$, in Eq. (9.2.2) is governed by Fick's law

$$\nabla^2 \delta C(r, t) = \frac{1}{D} \frac{\partial \delta C(r, t)}{\partial t} \tag{9.2.7}$$

where D is the translational diffusion constant and from the Stokes–Einstein relation can be expressed as

$$D = \frac{k_{\mathrm{B}} T}{6\pi R \eta} \tag{9.2.8}$$

where k_{B} is the Boltzmann constant, T is the absolute temperature, η is the viscosity of the medium, and R is the hydrodynamic radius of the diffusing particle. By measuring the diffusion constant, D, one can obtain the size of the particle. Equation (9.2.8) is valid for spherical particles, but with some approximation, it

applies to the particles that deviate from spherical symmetry. In many cases, the relative change in D, and not the absolute value of R itself, is the parameter of interest. From Eqs. (9.2.1), (9.2.7), and (9.2.8), the autocorrelation function for translational diffusion can be calculated as

$$G(\tau) = \frac{1}{N}\left[1 + \frac{\tau}{\tau_D}\right]^{-1}\left[1 + \frac{\tau}{\tau_D}\left(\frac{r_0}{z_0}\right)^2\right]^{-1/2} \tag{9.2.9}$$

where N is the mean number of particles in the effective observation volume and can be related to $\langle N\rangle$ by Eq. (9.2.6). The first term in Eq. (9.2.9) defines translational diffusion (xy-direction), and the second term, in z-direction. If diffusion occurs in two dimensions, the second term would be zero.

The translational diffusion, τ_D, is given by:

$$\tau_D = \frac{r_0^2}{4D} \tag{9.2.10}$$

Actually, the experimental value of D (Eq. (9.2.8)) can be obtained by measuring the translational diffusion constant, τ_D, of a molecule diffusing through axial radius, r_0, of excitation volume. Using a reference fluorophore sample for calibration with a known diffusion coefficient such as Rhodamine 6G ($D_{Rho} = 4.15 \times 10^{-6}$ cm^2 s^{-1}), the D_s of the molecule under investigation can be obtained as follows

$$D_s = \frac{\tau_{Rho}}{\tau_s} D_{Rho} \tag{9.2.11}$$

FCS measures τ_D by analyzing the fluorescence fluctuations obtained from excitation volume in an equilibrium solution. A least square fit of the model function, Eq. (9.2.9), to the experimental autocorrelation curve yields the free parameters, N, τ_D, and aspect ratio, $\omega = r_0/z_0$. If there are two different fluorescent particles A and B diffusing in the excitation volume, it is possible to calculate a cross-correlation function G_{AB} according to Eq. (9.2.1)

$$G_{AB}(\tau) = \frac{\langle \delta F_A(t+\tau)\delta F_B(t)\rangle}{\langle F_A(t)\rangle\langle F_B(t)\rangle} \tag{9.2.12}$$

If A and B are independently diffusing species, then G_{AB} is always zero. However, if they are associated with each other, G_{AB} is analogous to an autocorrelation function for this complex. Thus, cross correlation has the remarkable power of isolating signal from the complex AB even in a solution containing considerable amounts of free A and B.

9.2.2 Instrumentation

The FCS instrumentation depends on the type of experiment to be performed. So one should look for a multipurpose setup that can be easily modified without

much effort and expertise. Hence most people want to fabricate a homemade FCS setup. FCS measurement basically requires good focusing of the laser beam, next, efficient collection, and then, detection of collected fluorescence from the specimen with fast computation of the autocorrelation of the detected signal. There are two kinds of FCS instruments: one uses continuous wave excitation and the other uses pulsed excitation. FCS using pulsed excitation [32] has some advantages over the continuous wave FCS but it costs more due to the use of pulsed lasers. Picoquant [33] provides the best solution for time-gated time-resolved FCS microscopy. The company also provides components to upgrade various laser scanning microscopes, for example, Olympus, Nikon, Leica, and so on. Owing to the simplicity in fabrication, FCS using continuous wave laser has been described in this chapter. An FCS instrument should meet the following requirements: (i) best excitation of molecules in a small region of the sample, (ii) efficient collection of the fluorescence from that region, (iii) rejection of stray light and any background fluorescence, (iv) focusing the fluorescence into a pinhole, (v) detection of the fluorescence with a high quantum efficiency detector, and (vi) fast computation of the autocorrelation function of the obtained signal. The authors are describing here how to effectively implement these steps to bring the instrument in the working condition. An FCS instrument without microscope can be easily built in the laboratory with less effort. For nanoparticles' dynamics studies, a microscope is not required. Some companies are providing cheap FCS spectrometers with/without microscopes [33–36]. The required components with specifications can be found in well described method in Ref. [37]. If one wants measure in cells, a conventional fluorescence microscope would be necessary. A commercial confocal or multiphoton laser scanning microscope can also be modified for FCS measurements in a laboratory using the same components. The motivation for building an FCS instrument in-house, aside from considerable cost saving, comes from the extraordinary flexibility it offers the user in tailoring the instrument to particular experimental needs. Changing between different excitation lasers and different modes of excitation (single or multiphoton) requires interchange of different components and easy realignment of the instrument. Only homebuilt instrument allows a large flexibility to tailor it according to the requirement of the experimenter.

9.2.2.1 **Components of the Setup**

Before describing the optical design, the main components of the system are discussed first.

9.2.2.1.1 **Excitation**

The efficient detection of fluorescence from small illumination volume is the most crucial part of the FCS experiment. To achieve this, it is necessary to select appropriate excitation wavelength in order to get good emission from the sample. The tight focusing and exact shape of the focusing volume should be known in order to calculate the diffusion constant. For these reasons, lasers are the perfect light sources as they emit light with high degree of directionality and monochromaticity.

A Gaussian beam profile of a laser beam allows the estimation of focal volume. For single-photon experiments, low-power (<50 mW) continuous-wave lasers are sufficient. A multiline argon ion laser (blue at 488 nm and green at 514 nm) may extend the excitation choice. Lasers emitting in TEM_{00} mode are the ideal choice. Nowadays, cheap diode lasers are available in the market. The TEM_{00} mode from diode lasers can be achieved by the use of single-mode optical fiber.

For focusing the laser beam at the sample, a microscope objective lens is necessary. When working with samples in water medium and using silica glass as sample holder, water immersion objective with refractive index 1.2 is the best choice. Smaller spot size at the focus requires a larger beam diameter at the back aperture of the objective lens, implying that an expansion of the laser beam is usually necessary. The smallest focal volume can be achieved by overfilling the back aperture of the objective lens. The focus thus achieved is nearly diffraction limited, but the focal plane intensity distribution is not described by a simple analytical function. A Gaussian intensity distribution at the focal plane can be obtained by underfilling the back aperture of the microscope objective, but this yields a slightly larger observation area for the experiment.

9.2.2.1.2 **Collection**

The fluorescence emitted from the sample needs to be collected using the same microscope objective lens that is used for focusing the excitation beam. Higher NA of the lens ensures efficient collection of the fluorescence. In addition, this epifluorescence geometry automatically ensures that the collected fluorescence is decoupled from the forward-moving excitation light.

9.2.2.1.3 **Filters**

The fluorescence collected by a microscope objective needs to be separated from the excitation light path. A suitable dichroic, typically a multilayered coated dielectric thin film that transmits one range of wavelengths and reflects another range, optics is used for this purpose. A suitably selected dichroic reflects the excitation beam toward the microscope objective and transmits the fluorescence coming from the objective. After the dichroic, fluorescence filters are required. These are another specially coated optic designed to transmit light only within a small wavelength window. These two filters need to be chosen carefully to effectively cut off the excitation light and reduce the nonspecific background while maximizing the transmission of the fluorophore emission to the detector.

9.2.2.1.4 **Focusing to a Pinhole**

The next step is to focus the filtered fluorescence at the pinhole, and it can be done with a high-quality achromatic lens. Light originating from the focus passes through the pinhole aperture, while light from other regions is preferentially blocked. The probe volume in FCS experiments is a convolution of this detection profile with the illumination profile at the focal spot. Introducing a pinhole in the beam path is very critical, and an easy way is to use a multimode fiber, where the fiber face acts

as the pinhole. Changing the fiber allows easy alteration of the pinhole aperture size without the need for substantial realignment of the instrument.

9.2.2.1.5 Detection of the Fluorescence

The FCS measurements need very sensitive detectors, and the preferred detector is single-photon-counting APDs (avalanche photo-diodes). Silicon APDs have high quantum efficiency over a wide range in visible spectrum. The peak quantum efficiency of a Si-APD from PerkinElmer is >80%. The PicoQuant also provides APDs with high detection efficiency. Using a fiber-coupled APD makes the alignment and the light shielding of the instrument simpler. Data processing requires that the output of the detector be in the form of TTL (transistor-transistor logic) pulses. Photon-counting APDs and PMTs (photo-multiplier tubes) with built-in high-voltage (HV) power supply, amplifier, discriminator, and TTL logic output are easily available.

9.2.2.1.6 Analysis of the Detector Signal

The detector signal in form of either DC voltage or TTL pulses (in the case of pulsed excitation) is directly fed to a specialized digital signal processing card (autocorrelator card) housed in a personal computer that can perform quasi-real-time autocorrelation of the incoming signal. The commercially available autocorrelator cards are typically supplied with convenient driver software, which contain a few standard models for fitting limited types of FCS data. However, the data can be fitted with user-defined fitting models. In place of hardware correlators, the software correlators (data acquisition, DAQ cards) can also perform fast computing and contain the photon statistics. So these days, systems using DAQ cards are becoming more and more popular.

9.2.2.2 Construction of the Instrument

A ray diagram for the FCS instrument in the inverted geometry incorporating the components mentioned above is given in Figure 9.2.3, below.

The beam from laser aperture is first expanded by a combination of lenses L1 and L2 and then passed through aperture I2. An aperture is introduced between the combinations of lens to cut the diffracted light. Choosing the focal length depends on the laser beam diameter and back aperture diameter of the objective lens. The distance between the lenses adds up to the sum of their focal lengths to ensure proper beam collimation. The beam diameter is chosen to exactly fill the back aperture plane of the objective to achieve a minimal spot size with Gaussian profile in the sample. A filter wheel containing a series of neutral-density (ND) filters is placed in the excitation beam path so that the intensity of the excitation light can be easily adjusted. After ND filter, the expanded beam falls on the correctly chosen dichroic mirror (DM) and gets reflected vertically at right angle. Finally, the beam passes through high-NA water immersion objective. The objective focuses the light on the sample, and the redshifted fluorescence emanating from the sample is collected by the same objective, transmitted through the DM, and the falls on the mirror (M). The fluorescence is now filtered by emission filter (EM),

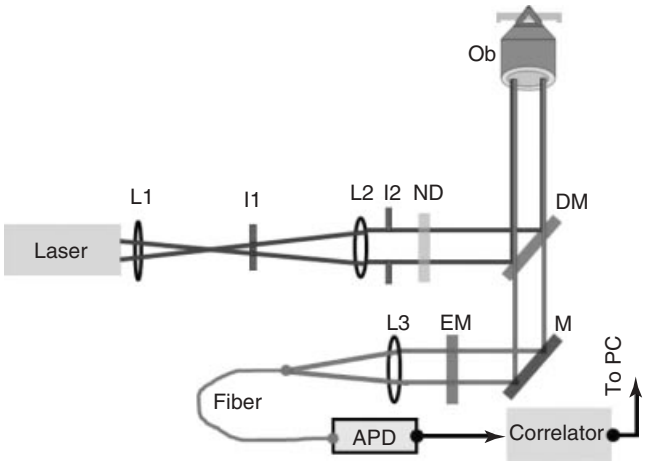

Figure 9.2.3 Block diagram of the proposed single-focus FCS.

focused by lens L3 (150 mm), and then coupled to the fiber through fiber coupler. The front face of the fiber will work as the pinhole or aperture. The fiber holder should allow the fiber to move, a few millimeters of translation along the radial (x and y) directions and 10 mm translation along the axial (z) direction. The other end of the fiber is connected with single-photon-counting detector (APD). The APD feeds signal to the data correlator card, which is connected to the computer. The excitation wavelength, the dichroic, and the EM filter must be chosen according to the excitation and emission spectra of the fluorescent probe used. The inverted geometry (Figure 9.2.3) is most suitable for liquid samples. The whole assembly needs to be mounted on a vibration-free optical bench. For a perpendicular deflection of the beam, cubic optical mounts housing rotatable dichroic holders are required. A fiber holder mount with three-axis movement is required for alignment.

For the cross-correlation experiments (investigating association of two kinds of particles having different emission wavelengths), an extra dichroic at an angle of 45° to the vertical axis is required. It will separate the two emission wavelength ranges. A second APD detector will be needed to couple the second emission to the second input channel of the autocorrelator card. The card can then either cross-correlate these two signals or autocorrelate them separately.

A spring-loaded sample mounting stage with micrometer-resolution vertical axis translation would be required to change the distance between the sample and the objective. The sample in the form of a droplet may be placed on a thin coverslip or on a coverslip-bottom petri dish on the sample stage. It requires very small amount of sample. The evaporation of the liquid may be prevented by covering the liquid droplet with a small dark cap and sealing it airtight with petroleum jelly or grease.

9.2.2.2.1 **FCS Setup with Microscope**

When FCS requires measurement inside the cell then an imaging setup is required (Figure 9.2.4). Any fluorescence microscope can incorporate FCS. Through

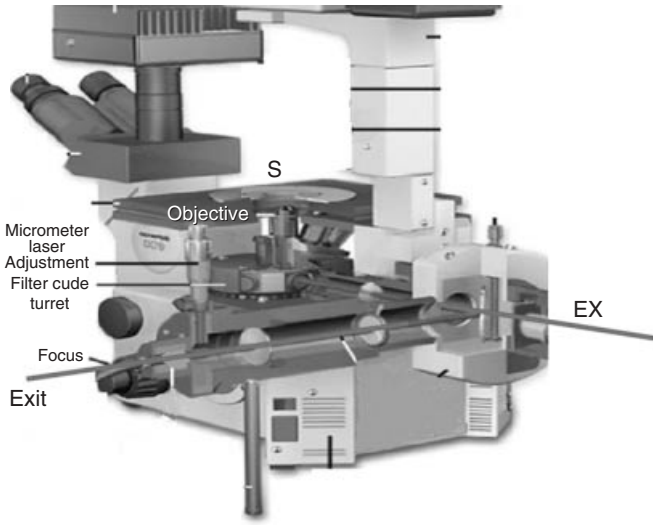

Figure 9.2.4 Optical path in the microscope (Olympus IX7).

fluorescence microscopy, an enlarged image of the sample can be obtained in transmission mode, and the laser spot defines the position of FCS measurement. Fluorescence microscopes, however, have lower resolution, and the FCS points cannot be taken with great accuracy. In order to achieve greater accuracy, a laser confocal scanning system could be used.

Instructions for modifying the Nikon TE300 inverted microscope can be found in Ref. [37]. A similar procedure can be adopted to modify other microscopes also. Here, in Figure 9.2.4, the optical path for Olympus IX7 inverted microscope is shown. The halogen lamp connected to the back port has been removed and is used for allowing entry of the laser light for FCS measurements. Outer diachroic mirror can be used to separate out the fluorescence. The side port is also available for the same, and either one works efficiently. Cells are plated on coverslip-bottom petri dishes mounted on the microscope stage. The focus can be moved along all three axes with precision, which allows us to choose the region of interest in the cells. The cells can be visualized using upper illumination and viewing through the eyepiece. While viewing the cells, utmost care should be taken to avoid scattered laser light from entering the eyes.

9.2.2.2.2 **Prism-Based Fluorescence Cross-Correlation Spectrometer (FCCS)**

Single-wavelength fluorescence cross-correlation spectrometers (SW-FCCSs) use conventional instrumentation including dichroic mirrors and emission filter sets to select the desired emission wavelengths or separate them into different detection channels as mentioned in the above setup. For multiple wavelength detection, multiple dichroics and emission filters will have to be used. This not only complicates

the setup but also amplifies the intensity losses because of nonideal transmission, principally surface reflections through each optical component. Commercially available emission filters and dichroics usually have broad spectral bandwidths and rise/fall bandwidths, respectively. Except each filter is designed to pass a limited wavelength region of the optical spectrum. The difficulty of balancing between optimizing signal detection and reducing spectral cross talk will increase with each additional detection channel. To overcome these problems, a dispersive element such as a diffraction grating could be used to spectrally separate the emission light.

For cross-correlation studies, prism-based spectrometer could be designed, constructed, and combined with an FCS system with single-laser excitation, and it is easy. Dispersion by the prism spectrometer causes a wavelength-dependent deflection angle such that the fluorescence signal can be focused on well-separated spots for the spectral ranges of interest. An optical fiber scanned through these foci selects different spectral ranges for detection and autocorrelation of standard and tandem dyes. The single fiber is then replaced with an optic fiber array to detect signals from two channels for cross correlation. This is an important step for detecting different kinds of nanoparticles and their interaction with each other in same media.

9.2.2.2.3 **Prism Spectrometer**

A schematic diagram of the prism-based fluorescence correlation spectrometer is shown in Figure 9.2.5. An argon-ion laser emitting at an excitation wavelength of 488 nm can be used for the excitation of several fluorophores. The laser beam diameter is expanded with two planar convex lenses L1 and L2 and coupled to the back aperture of the objective mounted onto a home-fabricated assembly or commercial setups. Fluorescence emission from the sample is collected by the objective and separated from the backscattered excitation light with a dichroic mirror (DM). The fluorescence is focused by the microscope tube lens L3 into the pinhole. An achromat L4 collimates the emission light, which then passes a 30° isosceles prism dispersing the fluorescence light. The focusing lens L5 brings the dispersed wavelengths into focus at different positions in the focal plane. A magnified image of the pinhole is formed for each wavelength, distributed in the image plane. The desired wavelength range is defined by the core diameter and the position of the optic fiber at the image plane.

There are several factors influencing the desired wavelength range to be detected: (i) The core diameter of the optic fiber acting as a slit for the spectrometer. The core diameter determines the spectral bandwidth, while the distance between the fiber cores determines the size of spectral channel separation. (ii) The focal length of the focusing lens. Longer focal length increases the linear deflection of the wavelengths at the image plane. (iii) The size or angle of the prism. A larger prism will have higher dispersion than a smaller prism. (iv) The spot size in the image plane. To achieve good spectral filtering, it is important to keep the ratio of the core diameter to spot diameter high while keeping the focusing NA below the acceptance angle of the fiber. For more details readers can go through Ref. [38].

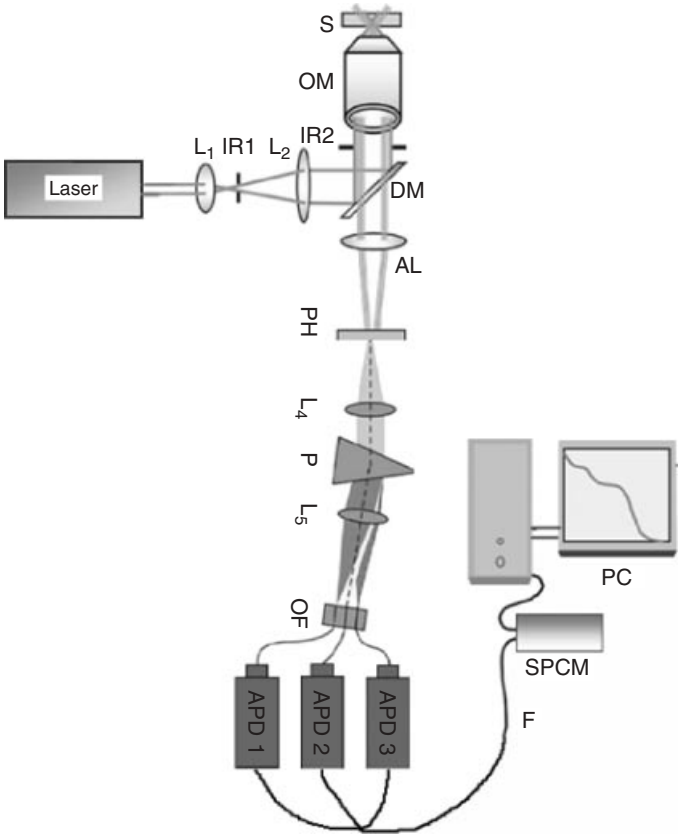

Figure 9.2.5 Optical setup of prism-based FCCS spectrometer.

9.2.3 Instrument Optimization and Performing FCS Experiments

9.2.3.1 Aligning and Optimizing the Setup

The laser beam used for excitation is made to pass through the center of all the optics and roughly through the center of two alignment irises IR1 and IR2 (Figure 9.2.3). IR1 is always present in the setup, while IR2 is placed in front of the objective holder during the initial alignment procedure. The expanded excitation beam is then collimated by adjusting the distance between the telescope lenses. The microscope objective is placed in this collimated beam path (after removing IR2). The beam axis needs to be aligned to the optical axis of the microscope objective lens. The excitation spot without the microscope objective lens in place is marked on a piece of paper placed in front. After the objective lens is placed, the divergent beam should be centered at this marked spot. This alignment is achieved by using the adjustment screws on the objective holder piece. The alignment on the detection

side is the most crucial. As stated earlier, the preferred way of performing FCS is with a fiber-coupled APD detector. The fiber face needs to be properly aligned with the focus of the fluorescence. Initially, the fiber is placed roughly at the distance where the focus of the achromat lens is estimated to be. Then, a concentrated solution (10^{-5} M) of a standard fluorescent dye (e.g., rhodamine B) can be used as the sample, and the fiber face is placed at the fluorescent spot, which is now easily visible. Then, the fiber holder's $x-y$ positioning is adjusted until the fluorescence couples to the fiber and can be seen at the other end of the fiber with the naked eye. Then, a very dilute (a few nanomolar) solution of the dye, which emits enough fluorescence to be easily detectable by the detector without damaging it, is used for the finer alignment. With this solution, the fluorescence and autocorrelation are measured as a function of the z-position (the fluorescence signal is maximized in x and y at each z-point). Finally, the fiber is placed at a position on the z-axis where fluorescence per particle (per-particle brightness) shows the maximum value. The sample placed on the microscope stage is then translated along the z-direction to find the appropriate distance between the sample and the objective lens. If there is a mismatch between the refractive indices of the immersion medium and the sample, the probe volume becomes progressively larger as the focus moves deeper into the sample. This lowers the autocorrelation magnitude. However, FCS experiments with solution specimens are conveniently carried out deep inside the sample, where the autocorrelation value does not change sharply with changes in the sample z-position. More details of the instrument parametric studies can be found in the Ref. [38]. Several other important requirements need to be fulfilled during the establishment of the instrument. These are discussed in the following sections.

9.2.3.1.1 Light Isolation

In FCS, the level of the detected signal can be much less than that emitted by a single molecule. So, even an apparently ''small'' amount of stray light can overwhelm the instrument and can damage the ultrasensitive detector. Black beam tubes are used to cover the space between the optics holders. The instrument skeleton is then wrapped with black electrical insulating tape to make it light tight. Special care is taken so that no light can leak around the band-pass-emission filter placed in front of the detector. In addition, the whole instrument with the detector is put inside a black cover box to allow experiments to continue under normal room light. Alignment of the fiber can be controlled with knobs outside the box that are connected to the micrometer adjustments of the fiber holder through steel cables. It is inconvenient to completely cover a microscope; hence, the experiments incorporating the microscope are carried out in a dark room.

9.2.3.1.2 Vibration Isolation

In FCS, we measure the fluctuation in the fluorescence caused by diffusive movement of molecules in a microscopic volume. This demands vibrationally isolated systems that can produce a stationary excitation spot. The instrument is mounted on a vibrationally isolated laser table after construction. If such a table is

not available, a heavy table with its feet placed in sandboxes can be used. A heavy optical breadboard (thick metal sheet with tapped holes in a square grid pattern) placed on a thick layer of foam on top of this table is well insulated from most of the vibrations.

9.2.3.1.3 Electrical Isolation

This is important if the laboratory's electrical supply is noisy. The detectors used for FCS measurements are very sensitive, prone to damage from light and electrical surges, and costly. A DC-to-DC converter, connected to a car battery, can supply power to the detectors, thus completely isolating the detectors from main fluctuations.

9.2.3.2 Preparing the Sample for FCS

The water to be used for making the sample solutions should be distilled twice before the experiment. Fluorescent dye solution for calibration purpose can be made by sonicating them in the required solvent using a tabletop sonicator. Sonication ensures that no aggregates are left in the sample.

9.2.4 Some FCS Studies on Nanomaterial Characterizations

In the recent years, several works have been done on the FCS studies of nanoparticles. These studies are becoming important because of the reasons mentioned in the Section 9.2.1. In the following paragraphs, some cases of the recent studies have been discussed.

Akcakir *et al.* [39] used FCS to measure the number density, brightness, and size of electrochemically etched Si into a colloid of ultrasmall blue luminescent nanoparticles. The results showed particle size of 1 nm, in close agreement with that obtained by direct imaging using transmission electron microscopy. They used mode-locked, femtosecond, titanium sapphire near-infrared laser, 150 fs duration at a repetition rate of 80 MHz, with average power around 20 mW at the target. The beam was focused on a spot of 0.7 μm diameter using a lens with NA 1.3, giving an average intensity of 5×10^6 W cm^{-2}. Fluctuations in the fluorescence signal were detected in photon-counting mode by either a photomultiplier or an APD. They measured fluorescence at the wavelength of second harmonic of excitation wavelength.

Neugart *et al.* [40] have studied the diffusion of diamond nanoparticles inside the cell. This is an area of increasing importance in modern life science. These types of studies can help to design new drug molecules for better efficiency. Various surface-coated metal nanoparticles have been used in the cell, but their cytotoxicity is a major concern. As an alternative, carbon or, more specifically, diamond nanoparticles, would be an option. The authors have used luminescent properties of defects in 40 nm sized diamond nanoparticles for their study. For cellular applications, the nanoparticle solution should be stable, and the authors have used different media to study the nanoparticle stability. Figure 9.2.6 shows the

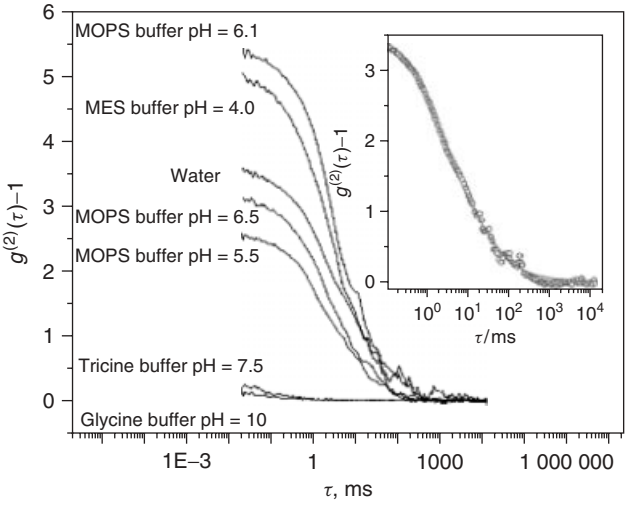

Figure 9.2.6 FCS curves of fluorescent nanodiamonds in different buffer solutions of different pH. Inset shows FCS curve in water with a numerical two-component fit.

correlation curves for different buffer solutions at various pH levels. It is apparent from the figure that the amplitude of the FCS curve depends on the pH value of the buffer solution. When pH becomes larger than 7.5, no correlation has been seen. The authors concluded that disappearance of the FCS curve at larger pH is because of nanocrystal aggregation. In the inset of Figure 9.2.6, the dual-component FCS fitting has been done for a sample in water buffer. Two decay times were obtained: one fast component of 2.5 ms and another slow component of 30 ms. It was found that the stability of the nanoparticles depends on the zeta potential. When the zeta potential becomes low, particle aggregation occurs. Further, to improve the stability of hydrosols, diamonds have been treated with sodium dodecyl sulfate (SDS) as a surfactant. Figure 9.2.7 shows an example of nanodiamonds in phosphate-buffered saline (PBS) buffer with and without SDS treatment. The authors found that nanodiamonds without surfactants precipitate in PBS buffer solutions, while those with SDS form a stable hydrosol.

The conclusion is that nanodiamonds with SDS form stable hydrosols in PBS at pH ranging between 5.7 and 7.8.

First, the authors used stable colloidal solution of these 40 nm sized nanoparticles inside HeLa cells to study the distribution and dynamics and found that nanoparticles got immobilized just after uptake by the cells. Next, they used 4 nm biotin-coated diamond nanoparticles along with streptavidin and found good correlation curve as shown in Figure 9.2.8.

Rochira *et al.* [41] studied CdSe/ZnS quantum dots through FCS and compared the photophysical properties with Alexa488 dye. They found that quantum dots showed numerous transitions between bright and dark states, especially at high

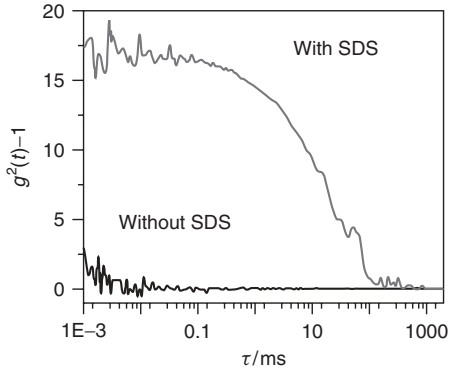

Figure 9.2.7 Diffusion of nanodiamonds with and without surfactant in phosphate-buffered saline (PBS) at pH = 7.2.

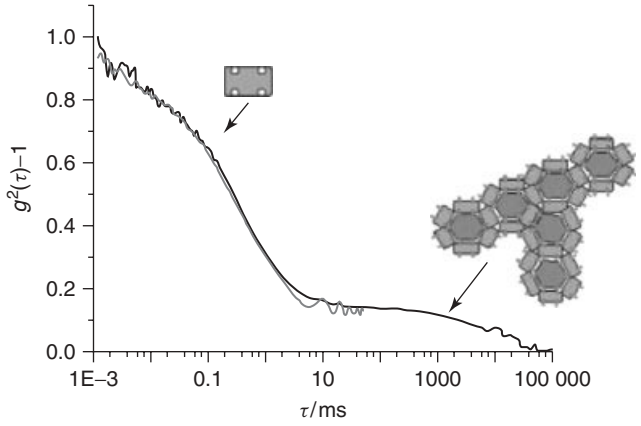

Figure 9.2.8 Correlation curve of biotinylated nanodiamonds in cells. Gray curve is Alexa488-labeled streptavidin alone. The first fast decaying part in the mixture is due to unbound streptavidin, and the slower component is due to the nanodiamonds bound with streptavidin.

illumination intensities and that the results suggested possibilities for significant improvement of quantum dots for biological applications by adjustments of manufacturing techniques and environmental conditions.

Ow *et al.* [42] studied the photophysical properties of core–shell silica particles through multiphoton FCS. They performed FCS measurements first on a series of parent fluorophores, cores, and core–shell particles made from a single synthesis and then on tetramethylrhodamine isothiocyanate (TRITC) dye and dye-based silica particles. They found that although containing multiple fluorophores, the per-particle brightness of the cores is less than that of core–shell particles and the free dye molecules (Figure 9.2.9). They also demonstrated that the addition of

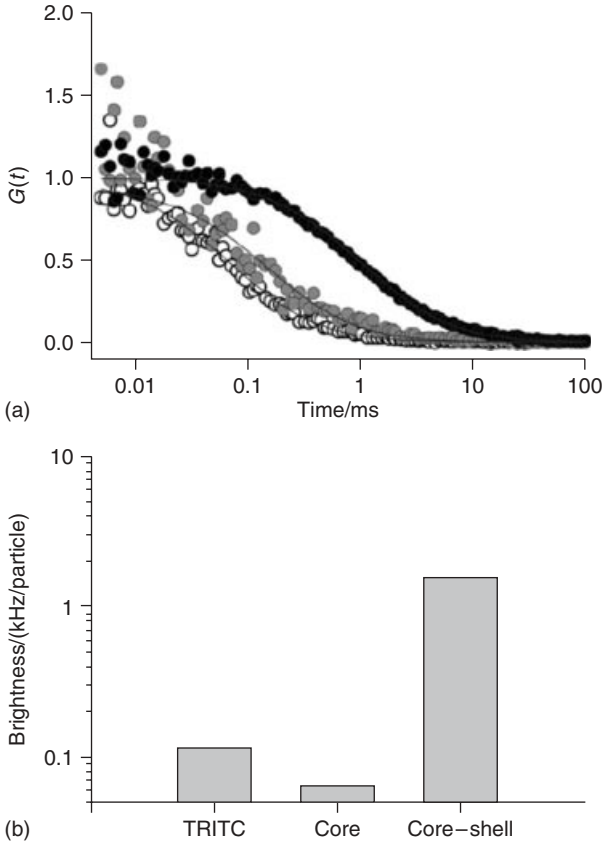

Figure 9.2.9 (a) FCS autocorrelation curves for free TRITC dye (white), TRITC-based silica core particles (gray), and 30 nm core–shell TRITC-based silica nanoparticles (black) and (b) a comparison of per-particle brightness values for TRITC dye, core particles, and core–shell nanoparticles.

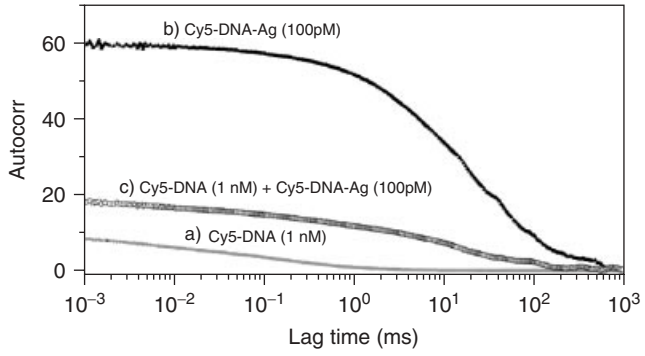

Figure 9.2.10 Autocorrelation of Cy5-DNA, bound to a silver particle and the mixture.

the silica shell onto the core significantly enhances the brightness of the core–shell particles.

Ray *et al.* [43] have used fluorescence lifetime correlation spectroscopy (FLCS) to separate the FCS contributions from fluorophores and metal-conjugated fluorophores. They suggest that FLCS is a powerful method for investigating metal–fluorophore interaction at the single molecule level and for separating two different species from a mixture solution emitting at the same wavelength. Figure 9.2.10 shows the measured correlation functions for free Cy5-DNA (1 nM), Cy5-DNA-Ag-particle (100 pM), and a mixture of both in solution. The correlation function for the bound Cy5 can be seen to be strongly shifted to longer times because of the slower diffusion of the Cy5-DNA-Ag-particle as compared to the free Cy5-DNA.

9.2.5 Conclusions and Future Prospects

FCS is a laser spectroscopic tool whose versatility and ease of implementation has opened up new possibilities to understand the behavior of molecules at the single-molecule level. Nanoparticles can be studied well with this technique. It is minimally invasive due to use of low-power light radiation, and is thus extremely useful for investigating soft biological systems. As this method is concerned with fluctuations around the thermodynamic equilibrium, no external stress has to be applied to determine the relaxation parameters. The confocal setup promises high spatial resolution, which is combined with its inherently high temporal resolution to render it complementary to most other fluorescence techniques. A large number of parameters can be determined by FCS, among them the mobility constants and concentrations, fast internal dynamics, and photophysical processes.

This chapter discusses FCS introduction, experimental technique, and its potential in nanomaterials characterization. However, the possibilities are vast and in future, there will be new testing of its instrumentation and research on understanding of nanoparticle photophysics. After Medge *et al.* (1974), many improvements in the technique have been made, but there is still room for more improvement. Very recently, dual-focus FCS technique has been introduced, which provides us absolute diffusion constant of diffusing molecules and has also made it possible to measure unknown focal volume [45, 46]. Also, the necessary condition that nanoparticle/molecule must be fluorescent during FCS measurement has been eliminated by the introduction of new PhCS. FCS studies on nanomaterials demand much attention since nowadays medical science utilizes more and more nanoparticles. A clear understanding is necessary to eliminate after-use health risks, and FCS is the most suitable tool for this.

Acknowledgments

Kaushal Kumar gratefully acknowledges the Italian Institute of Technology (IIT), Genova, Italy, for financial support.

References

1. Hodge, G.A., Bowman, D., and Ludlow, K. (eds) (2007) *New Global Frontiers in Regulation: the Age of Nanotechnology*, Edward Elgar Publishing.
2. Roco, M.C. (1999) Nanoparticles and nanotechnology research. *J. Nanopart. Res.*, **1**, 1.
3. Roco, M.C. (2003) Nanotechnology: convergence with modern biology and medicine. *Curr. Opin. Biotechnol.*, **14**, 337.
4. Kawasaki, E.S. and Player, A. (2005) Nanotechnology, nanomedicine, and the development of new, effective therapies for cancer. *Nanomed. Nanotechnol. Biol. Med.*, **1**, 101.
5. Sahoo, S.K., Parveen, A.S., and Panda, J.J. (2007) The present and future of nanotechnology in human health care. *Nanomed. Nanotechnol. Biol. Med.*, **3**, 20.
6. Gaoa, J. and Xu, B. (2009) Nano, applications of nanomaterials inside cells. *Nano Today*, **4**, 37.
7. Rodriguez, J.A. and Garcia, M.F. (2007) *Synthesis, Properties, and Applications of Oxide Nanomaterials*, Wiley-Interscience, Hoboken, NJ.
8. Colvin, V.L. (2003) The potential environmental impact of engineered nanomaterials. *Nat. Biotechnol.*, **21**, 1166.
9. Hoet, P.H.M., Brüske-Hohlfeld, I., and Salata, O.V. (2004) Nanoparticles-known and unknown health risks. *J. Nanobiotechnol.*, **2**, 12.
10. Oberdorster, G., Stone, V., and Donaldson, K. (2007) Toxicology of nanoparticles: a historical perspective. *Nanotoxicology*, **1**, 2–25.
11. Oberdörster, G., Oberdörster, E., and Oberdörster, J. (2005) Nanotoxicology: an emerging discipline evolving from studies of ultrafine particles. *Environ. Health Perspect.*, **113**, 823.
12. Oberdörster, G. (2001) Pulmonary effects of inhaled ultrafine particles. *Int. Arch. Occup. Environ. Health*, **74**, 1.
13. Bruchez, M., Moronne, M., Gin, P., Weiss, S., and Alivisatos, A.P. (1998) Semiconductor nanocrystals as fluorescent biological labels. *Science*, **281**, 2013.
14. Mah, C., Zolotukhin, I., Fraites, T.J., Dobson, J., Batich, C., and Byrne, B.J. (2000) Microsphere- mediated delivery of recombinant AAV vectors in vitro and in vivo. *Mol. Ther.*, **1**, S239.
15. Edelstein, R.L., Tamanaha, C.R., Sheehan, P.E., Miller, M.M., Baselt, D.R., Whitman, L.J., and Colton, R.J. (2000) The BARC biosensor applied to the detection of biological warfare agents. *Biosens. Bioelectron.*, **14**, 805.
16. Nam, J.M., Thaxton, C.C., and Mirkin, C.A. (2003) Nanoparticles-based bio-bar codes for the ultrasensitive detection of proteins. *Science*, **301**, 1884.
17. Mahtab, R., Rogers, J.P., and Murphy, C.J. (1995) Protein-sized quantum dot luminescence can distinguish between "straight", "bent", and "kinked" oligonucleotides. *J. Am. Chem. Soc.*, **117**, 9099.
18. Ma, J., Wong, H., Kong, L.B., and Peng, K.W. (2003) Biomimetic processing of nanocrystallite bioactive apatite coating on titanium. *Nanotechnology*, **14**, 619.
19. Yoshida, J. and Kobayashi, T. (1999) Intracellular hyperthermia for cancer using magnetite cationic liposomes. *J. Magn. Magn. Mater.*, **194**, 176.
20. Weissleder, R., Elizondo, G., Wittenburg, J., Rabito, C.A., Bengele, H.H., and Josephson, L. (1990) Ultrasmallsuperparamagnetic iron oxide: characterization of a new class of contrast agents for MRimaging. *Radiology*, **175**, 489.
21. Luo, D. and Saltzman, W.M. (2000) Synthetic DNA delivery systems. *Nat. Biotechnol.*, **18**, 33.
22. Berciaud, S., Lasne, D., Blab, G.A., Cognet, L., and Lounis, B. (2006) Photothermal heterodyne imaging of individual metallic nanoparticles: theory versus experiment. *Phys. Rev.*, **B73**, 045424.
23. Plakhotnik, T., Donley, E.A., and Wild, U.P. (1997) Single molecule spectroscopy. *Annu. Rev. Phys. Chem.*, **48**, 181.

24. Moerner, W.E. (2002) A dozen years of single-molecule spectroscopy in physics, chemistry, and biophysics. *J. Phys. Chem. B*, **106**, 910.
25. Magde, D., Elson, E., and Webb, W.W. (1972) Thermodynamic fluctuations in a reacting system--measurement by fluorescence correlation spectroscopy. *Phys. Rev. Lett.*, **29**, 705.
26. Octeau, V., Cognet, L., Duchesne, L., Lasne, D., Schaeffer, N., Fernig, D.G., and Lounis, B. (2009) Photothermal absorption correlation spectroscopy. *ACS Nano*, **3**, 345.
27. Paulo, P.M.R., Gaiduk, A., Kulzer, F., Gabby Krens, S.F., Spaink, H.P., Schmidt, T., and Orrit, M. (2009) Photothermal correlation spectroscopy of gold nanoparticles in solution. *J. Phys. Chem. C*, **113**, 11451.
28. Thompson, N.L. (1991) *Topics in Fluorescence Spectroscopy: Techniques*, Plenum Press, New York, pp. 337–378.
29. Larson, D.R., Zipfel, W.R., Williams, R.M., Clark, S.W., Bruchez, M.P., Wise, F.W., and Webb, W.W. (2003) *Science*, **300**, 1434.
30. Qian, H. and Elson, E. (1991) Analysis of confocal laser-microscope optics for 3-d fluorescence correlation spectroscopy. *Appl. Opt.*, **30**, 1185.
31. Rigler, R., Mets, U., Widengren, J., and Kask, P. (1993) Fluorescence correlation spectroscopy with high count rate and low background-analysis of translational diffusion. *Eur. Biophys. J.*, **22**, 69.
32. Wahl, M.B.M., Rahn, H.J., Erdmann, R., and Enderlein, J. (2002) Time-resolved fluorescence correlation spectroscopy. *Chem. Phys. Lett.*, **353**, 439.
33. *http://www.picoquant.com/*.
34. *http://www.iss.com/microscopy/instruments/albaFCS.html*.
35. *http://www.fcsxpert.com/products/fluorescence-correlation-spectrometer.html*.
36. *http://sales.hamamatsu.com/en/products/system division/spectroscopy/fluorescence-correlation-spectroscopy.php*.
37. Sengupta, P., Balaji, J., and Maiti, S. (2002) Measuring diffusion in cell membranes by fluorescence correlation spectroscopy. *Methods*, **27**, 374.
38. Chin, H.L. (2006) *Development of a fluorescence correlation spectroscopy method for the study of biomolecular interactions*, Ph. D. Thesis, Department of Chemistry, National University of Singapore.
39. Akcakir, O., Therrien, J., Belomoin, G., Barry, N., Muller, J.D., Gratton, E., and Nayfeh, M. (2000) Detection of luminescent single ultrasmall silicon nanoparticles using fluctuation correlation spectroscopy. *Appl. Phys. Lett.*, **76**, 1857.
40. Neugart, F., Zappe, A., Jelezko, F., Tietz, C., Paul Boudou, J., and Wrachtrup, A.K.J. (2007) Dynamics of diamond nanoparticles in solution and cells. *Nano Lett.*, **7**, 3588.
41. Jennifer, A., Rochira, A., Gudheti, M.V., Gould, T.J., Laughlin, R.R., Nadeau, J.L., and Hess, S.T. (2007) Fluorescence intermittency limits brightness in CdSe/ZnS nanoparticles quantified by fluorescence correlation spectroscopy. *J. Phys. Chem. C*, **111**, 1695.
42. Ow, H., Larson, D., Srivastava, M., Baird, B., Webb, W., and Wiesner, U. (2005) Bright and stable core-shell fluorescent silica nanoparticles. *Nano Lett.*, **5**, 113.
43. Ray, K., Zhang, J., and Lakowicz, J.R. (2009) Fluorophore conjugated silver nanoparticles: a time-resolved fluorescence correlation spectroscopic study. *Proc. Soc. Photo. Opt. Instrum. Eng.*, **7185**, 71850C, doi: 10.1117/12.808958
44. Magde, D., Elson, E.L., and Webb, W.W. (1974) Fluorescence correlation spectroscopy-II. An experimental realization. *Biopolymers*, **13**, 29.
45. Korlann, Y., Dertinger, T., Michalet, X., Weiss, S., and Enderlein, J. (2008) Measuring diffusion with polarization-modulation dual-focus fluorescence correlation spectroscopy. *Opt. Express*, **16**, 14609.
46. Didier, P., Godet, J., and Mély, Y. (2009) Two-photon two-focus fluorescence correlation spectroscopy with a tunable distance between the excitation volumes. *J. Fluoresc.*, **19**, 561.

9.3
Time-Resolved Photoluminescence Spectroscopy of Nanomaterials

Yashashchandra Dwivedi

9.3.1
Introduction

Spectroscopic characterizations of materials basically deal with the problems that explore the molecular structure and relaxation dynamics of the excited species. To determine the molecular structure, eigenstates of total Hamiltonian and position of defect level, typical optical processes such as absorption, emission, and scattering were analyzed using several techniques such as UV–Vis–NIR absorption, FT-IR, photoluminescence, thermoluminescence, cathodoluminescence, X-ray spectroscopy, Raman scattering, and so on. However, the investigation of the relaxation process is multifaceted because of the possible interaction of excited molecules/ions (via intramolecular or intermolecular), which leads to redistribution of excited species and significantly affects the radiative relaxation process and consequently the variation observed in photoluminescence intensity. Hence it is highly desirable to understand the relaxation dynamics of excited species, which is possible by using the time-resolved photoluminescence (TRPL) technique. TRPL is a nondestructive, unique way of studying materials because the temporal information combined with spectral data can elucidate the dynamics of carriers involved in optical transitions.

In photoluminescence spectroscopy, the energy needed to change the electron distribution in a molecule is of the order of several electron volts; consequently, the photons used to excite the sample should have higher energies (or at least of this order), so that these can impart excess energy into the material in a process called *photoexcitation*. One way by which this excess energy can be dissipated by the sample is through the emission of light or photoluminescence. Photoluminescence includes radiative and nonradiative processes. A radiative process involves the molecule losing its excitation energy as a photon, while in the nonradiative process the excess energy is transformed into heat that can be measured in a variety of ways, for example, thermal lensing or photoacoustic techniques. As shown in Figure 9.3.1, the fluorescent state of a molecule can directly decay to the ground state (resonance fluorescence) or a lower state through a process called *internal conversion*, before radiatively dropping to the ground state (fluorescence). It can also decay nonradiatively through a process termed *intersystem crossing* to a triplet state in a radiationless transition. This naturally causes a longer duration between excitation and emission, and because of longer duration of the emission, a delayed fluorescence is sometimes observed even after several minutes.

Although analysis of relaxation processes in an organic molecule and in nanostructured material should not be treated in the same way, various optical processes involved in the loss of excitation energy can be understood on the basis of a Jabolonski-like diagram (Figure 9.3.1). Typically, decay of photoexcited valence

Nanomaterials: Processing and Characterization with Lasers, First Edition.
Edited by Subhash Chandra Singh, Haibo Zeng, Chunlei Guo, and Weiping Cai.

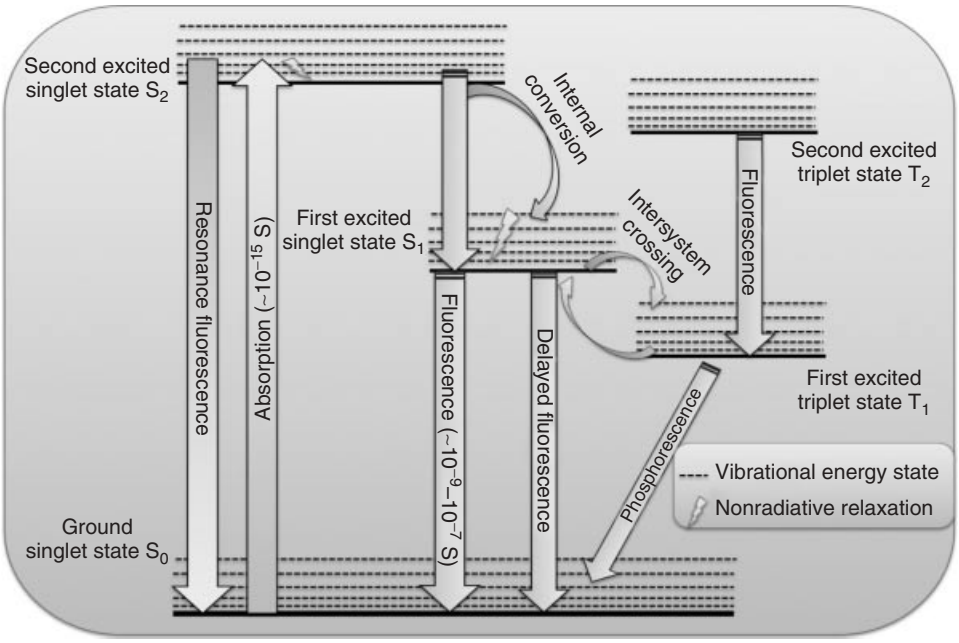

Figure 9.3.1 Jabolonski-like diagram and the different radiative and nonradiative relaxation processes in an organic molecule.

electrons takes place within 10^{-3}–10^{-9} s, while high-energy atomic states populated by inner shell excitation decay in a much shorter time (10^{-15} s). The transition between states of same parity (symmetry) may persist for approximately milliseconds. Relaxation of excited electrons in metals or semiconductor materials occurs within a timescale of 10^{-13}–10^{-15} s, and excited states of atomic nuclei can even decay in times shorter than 10^{-18} s. In case of intermolecular interaction, energy of one excited species is transferred to another neutral or excited species in the timescale of $\sim 10^{-9}$–10^{-15} s, although the time required is typically a function of concentration, distance between the interacting species, temperature and so on.

Owing to nonradiative processes, intensity of radiative emission gets quenched. Excited species can lose their excitation by nonradiative process either through the aid of coupled vibrational and electronic energy states or through collisions with other atoms or molecules. The former process is known as *static quenching*, while the latter is termed as *dynamic quenching*.

When a material is illuminated by a laser or lamp, a small population of ground state atoms or molecules is excited. Let us assume that on excitation with laser, a temporary concentration of excited-state molecules [X^*] at some moment in time is generated. Let us further assume that X^* is strongly fluorescent and that we can follow the intensity of this fluorescence later using a sensitive light detector such as a photomultiplier tube or semiconductor diodes. If there are no quenching agents present in the system (i.e., in the absence of species that can quench the

fluorescence through collisions) then X^* can return to the ground state through a normal fluorescence (Eq. (9.3.1)) emitting a photon of energy $h\nu$ or by a nonradiative decay process (Eq. (9.3.2)) through coupling of vibrational and electronic levels.

$$X^* \xrightarrow{K_1} X + h\nu \tag{9.3.1}$$

$$X^* \xrightarrow{K_2} X \tag{9.3.2}$$

where k_1 and k_2 are the rate constants for radiative and nonradiative processes. If only these two paths to the ground state are available, the rate equation for $[X^*]$ can be written as

$$\begin{aligned} \frac{\mathrm{d}[X^*]}{\mathrm{d}t} &= -k_1[X^*] - k_2[X^*] \\ \frac{\mathrm{d}[X^*]}{\mathrm{d}t} &= -\left(k_1 + k_2\right)[X^*] \end{aligned} \tag{9.3.3}$$

On integrating Eq. (9.3.3) with respect to presume conditions $t = 0$ and $[X^*] = [X^*]_0$ results in

$$[X^*] = [X^*]_0\, \mathrm{e}^{-(k_1+k_2)t} \tag{9.3.4}$$

It is evident that the rate constants k_1 and k_2 quantify the relaxation rate. Hence, fluorescence lifetime in the absence of a quencher can be expressed as

$$\tau_0 = \frac{1}{\left(k_1 + k_2\right)} \tag{9.3.5}$$

Summing the expressions (9.3.4) and (9.3.5),

$$[X^*] = [X^*]_0\, \mathrm{e}^{-t/\tau_0} \tag{9.3.6}$$

Through this way, fluorescence lifetime (τ_0) can be defined as the amount of time that it takes for the fluorescence intensity to decay to 1/e of its initial value. τ_0 is the mean spontaneous lifetime of the state, which is related to the total transition probability A by $A = 1/\tau_0$. Typical values of the lifetime of excited valence electrons lie in the nanosecond range. In the presence of a quenching species (Q), a third process will come into play, which enforces an excited species X^* to relax to the ground state through nonradiative process

$$X^* + Q \xrightarrow{K_\mathrm{q}} X \tag{9.3.7}$$

Including Eq. (9.3.7), the rate equation for $[X^*]$ (Eq. (9.3.3)) becomes

$$\frac{\mathrm{d}[X^*]}{\mathrm{d}t} = -\left(k_1 + k_2 + k_\mathrm{q}\left[Q\right]\right)[X^*] \tag{9.3.8}$$

where k_q is the quenching constant. Assuming $[Q] \gg [X^*]$ and integrating Eq. (9.3.8), we have

$$[X^*] = [X^*]_0\, \mathrm{e}^{-(k_1+k_2+k_\mathrm{q}[Q])t} \tag{9.3.9}$$

Hence, the fluorescence lifetime in the presence of the quencher will be

$$\tau = \frac{1}{(k_1 + k_2 + k_q[Q])} \tag{9.3.10}$$

Equation (9.3.6) represents the ideal case where the excitation pulse is infinitely narrow. If the pulse has a finite width, the exponential fluorescence decay (Eq. (9.3.6)) will be convoluted with the pulse profile function $B(t)$, resulting in the following more general expression

$$[X^*] = [X^*]_0 \int_0^t B\left(t - t'\right) e^{-t'/\tau_0} dt' \tag{9.3.11}$$

Considering the case of nanomaterials, nonradiative transition may be influenced in the presence of defect sites, size, and shape of the nanostructure and the ambient conditions. As the size approaches the exciton Bohr radius, optical properties critical to device applications, such as bandgap and photoluminescence lifetime, are affected greatly because of the quantum confinement effect [1–3]. In response of confinement, excitons in geometrically confined systems exhibit different properties as compared to three-dimensional excitons [4, 5].

Excitation of a nonequilibrium density of electrons and holes, excitons, or any other number of quasi-particles will ultimately lead to the recombination and simultaneous emission of photons, and this is called *radiative recombination*. If the recombination proceeds with the emission of phonons instead of photons, then the recombination is termed as *nonradiative recombination*. Detailed information about the different recombination processes can be accessed from Refs. [6, 7]. Both radiative and nonradiative rate of recombination affect the observed luminescent intensity. Recalling Eq. (9.3.5), a photoluminescence decay rate is a sum of the radiative and nonradiative decay rates

$$\frac{1}{\tau_{\text{Lifetime}}} = \frac{1}{\tau_{\text{Radiative}}} + \frac{1}{\tau_{\text{Nonradiative}}} \tag{9.3.12}$$

Radiative and nonradiative processes are competitive processes among which the process that dominates can be estimated by TRPL using suitable reference material. Since nonradiative processes are thought to be more likely at the surface, the effective lifetime is often written as a combination of surface and bulk lifetimes [8]

$$\frac{1}{\tau_{\text{eff}}} = \frac{1}{\tau_{\text{bulk}}} + \frac{1}{\tau_{\text{surf}}} \tag{9.3.13}$$

The transformation of the bulk material into nanostructures can enhance nonradiative surface-mediated trapping through defect states and collisional effects. Such effects, including Auger recombination [9], can also occur on a short timescale, competing with radiative decay [10]. In addition, nonradiative processes in the system invoked by changing the defect concentration of the sample in such a way that the concentration increases linearly over the growth time, and surface states cause nonradiative decay. Stimulated emission can also influence the short time dynamics, often obscuring nonradiative decay mechanisms [11].

Size-dependent radiative decay can be differentiated into three different regions [12]:

1) If a nanoparticle is smaller than the Bohr diameter of the exciton, quantum confinement effect may lead to size-dependent oscillator strength.
2) If a nanoparticle is bigger than the exciton Bohr radius but smaller than the wavelength of the light, then scattering with the surface provides a path for an exciton to decay radiatively.
3) If the size of the nanoparticle approaches the dimension of the wavelengths, exciton polariton effects come into play.

Theoretical analysis showed that the rate of radiative recombination decreases as the size increases in regions (1) and (3), whereas it behaves oppositely in region (2) [13]. According to the computational result for a quantum dot including the exciton–polariton effect, the size-dependent recombination rate is

$$\Gamma_0 = \frac{\sqrt{2\pi}}{12}\omega_{LT}\left(\frac{2\pi}{\lambda_0}\right)^3 \langle r\rangle^3 \exp\left(-8 \in_b \frac{\pi^2\langle r\rangle^2}{\lambda_0^2}\right) \tag{9.3.14}$$

Here, ε_b is the dielectric constant, ω_{LT} the longitudinal–transverse splitting frequency, and $<r>$ the size (1/e) of the exciton wave function. For a nanosphere radius of 17 nm, ω_{LT} is 1 meV and λ_0 is 350 nm and there is a minimum radiative lifetime; 260 ps is obtained for a nanosphere radius of 17 nm, and it increases monotonically as the size increases [12]. In addition, the perturbation of the electron and hole states by quantum confinement produces unique dynamics that are strongly dependent on the nanoparticle size [14].

The strain in crystal could be clearly evidenced by several techniques, namely, shifts in the photoluminescence, photoreflectance, and line positions [15, 16]. As the energy of the free exciton associated with the top valence band varies linearly with the in-plane and axial components of the strain tensor, lifetime could be a good tool to predict the expected strain in the crystal lattice [16]. TRPL measurements could be an additional measure of crystal quality to correlate sample thickness with incorporated strain. TRPL decay measurements on the samples showed that radiative lifetime increased as the sample thickness increased, verifying that the crystal quality improves with reduced strain [17].

9.3.1.1 Example

In case of high-quality GaN crystals grown on sapphire by hydride vapor-phase epitaxy, the thermal expansion mismatch between sapphire and GaN produces strain in the GaN crystal as it is cooled from the growth temperature to room temperature. The variation in lifetimes for transition energies of both the *A* free exciton energies and a neutral-donor-bound exciton ($D + X$) as a function of strain is given in Figure 9.3.2 [18].

The decay data display single exponential decays for all of the transitions over several times the radiative recombination lifetime. The D^0, X lifetime is greater than the free exciton lifetime as is usually observed [19]. The lifetime increases with sample thickness, as the surface strain decreases. This suggests that the factors

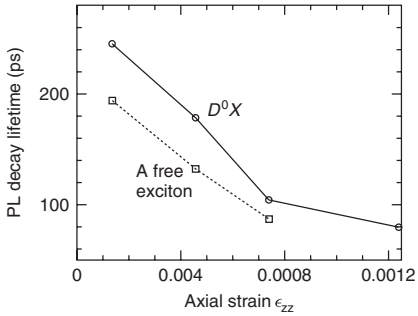

Figure 9.3.2 Decay lifetimes of the A-band free exciton and the donor-bound exciton as a function of the axial strain ϵ_{zz}. PL, photoluminescence [18].

contributing to strain also introduce recombination paths as well as nonradiative decay processes. Slower exciton decay was also observed when the layer thickness was increased in MOCVD-grown GaN [20].

9.3.2
Experimental Methods of TRPL

To measure the lifetime of the emitting state, two techniques are known, that is, time-domain techniques and frequency-domain techniques. The time-domain techniques are direct techniques. It measure fluorescence decay curves (i.e., fluorescence intensity as a function of time) directly and estimate lifetime by proper exponential fitting function of the obtained decay curve. The phase technique is totally different from that of the former in terms of measurement and the method of detection. It utilizes a sinusoidally modulated light for the excitation of the fluorescence. The emitted light also becomes modulated at the same frequency, but it will show some shift (delay) relative to the excitation light. This shift is called a *phase shift*, and it contains the information about the lifetime. Depending on the lifetime, the fluorescence will show a decreased depth of the sinusoidal modulation relative to the excitation light.

In practice, it is difficult to specify the lower limit of the lifetime that can be measured by an instrument. Factors such as quantum yield, fluorophore concentration, and decay kinetics can affect the measurement. In order to demonstrate performance, one must use a well-characterized standard or propose a special convincing protocol. TRPL is measured by exciting luminescence from a sample with a pulsed light source, and then measuring the subsequent decay in photoluminescence as a function of time. The time resolution achieved is determined by the quality of excitation source and the detector. A wide variety of experimental configurations can accomplish this. Most experiments excite the sample with a pulsed laser source and detect the photoluminescence with a photodiode, streak camera, or photomultiplier tube set up for upconversion or single-photon counting. The system response time, wavelength range, sensitivity, operational difficulty, and

cost vary widely for each configuration. In order to obtain precise fluorescence lifetime, the profile of instrument response function (IRF) (excitation pulse) has to be measured in addition to the fluorescence decay. This is because the lamp (or laser) pulse has a finite-temporal width, which distorts the intrinsic fluorescence decay response from the sample. This effect is called *convolution*. In a typical experiment, two curves are measured: the IRF using a scatterer solution and the decay curve. Analysis is then performed by convoluting the IRF with a model function (e.g., a single exponential decay or a double exponential decay or some other function) and then comparing the result with the experimental decay. This is done by an iterative numerical procedure until the best agreement with the experimental decay curve is achieved.

In case of nanosecond lifetime measurements, digital storage oscilloscopes with sample rates higher than 1 Gs s^{-1}, which follow the electrical signal with a time resolution of nanoseconds, are used. It can be used for single-shot and repetitive events. The time resolution of only a few nanoseconds can be achieved with this system. A boxcar integrator stores the signal during a time window. This apparatus is mainly used for the gating of the temporal signal with a low repetition rate up to 1 KHz, for example, pump-probe experiments using a regenerative amplifier. It is used for repetitive events, and subnanosecond time resolution can be measured.

Time-resolved measurements in picosecond resolution are performed by making use of time resolution of detectors. In recent times, pump-probe photoinduced absorption, single-photon counting, photoluminescence upconversion, and photoluminescence imaging techniques are mostly used for picosecond lifetime measurements. These techniques have been tremendously exploited to probe exciton dynamics, energy transfer, and radiative decay channels in organic and nanomaterials. For these experiments, a laser with a broad spectral gain profile is used as a light source, and the wavelength is tuned across the gain profile by wavelength-selecting elements (such as prisms, gratings, or interferometers) inside the laser cavity. For this, Ti:sapphire lasers of femtosecond pulse width, which pump by continuous argon ion laser or green laser source, are used. An optical frequency tripler further extends this range to include 233–327 nm. Additional excitation wavelengths are obtained using a harmonic generator for frequency doubling and tripling or an optical parameter oscillator. The pulse energy of Ti:sapphire can be improved by the conventional amplification method in which population of gain medium is inverted while pumped by a powerful laser or by parametric amplification. In case of optical parametric amplification, nonlinear optical crystals are used, which split pump photon into two photons, called the *signal and idler*; both the signal and the idler can be tuned over a wide range in the visible or infrared region, by seeding the system with a wavelength-tunable laser and/or by using an optical parametric oscillator and changing the phase-matching conditions of the crystal. The laser repetition rate can be lowered by a pulse picker . An acousto-optic pulse picker is used to lower the laser pulse rate for longer lifetime fluorophores. A brief introduction of the different techniques used for TRPL spectroscopy is discussed in the following sections.

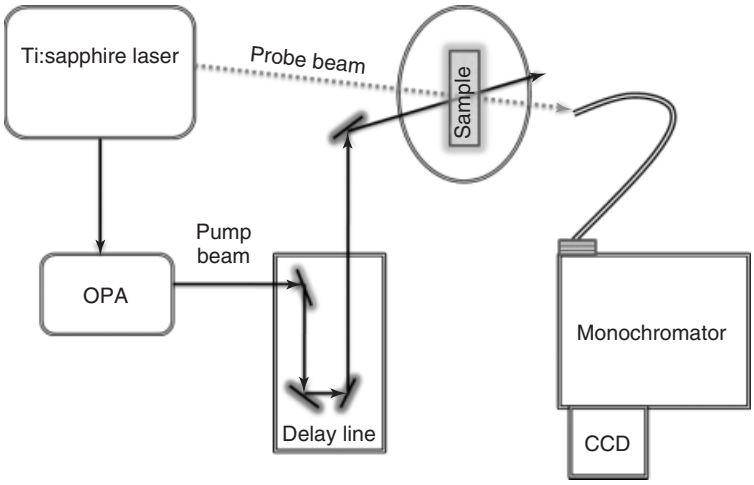

Figure 9.3.3 A schematic diagram of the pump-probe method.

9.3.2.1 **Pump-Probe Technique**

The pump-probe technique is the most commonly used technique to study transient phenomena. This technique needs simple optical pathways and detection with the advantage to probe transients up to the laser pulse width. The technique uses two femtosecond beams: a pump to initiate absorption in the sample and a probe beam, which is a fraction of the pump at a different wavelength, entering the sample at a later time delay and monitors an optical property. By sweeping the time delay between the pump and probe pulses using a variable optical delay line placed on the pump beam optical pathway, it is possible to assemble measurements as a function of time. The wavelength of the excitation pulse (pump) is chosen by adjusting the nonlinear crystal of an optical parametric amplifier (OPA). The probe pulse is typically a UV, visible, or infrared pulse in which a snap-shot spectrum is taken as a function of the delay time. Often, the probe pulse is generated from a portion of the excitation beam, but it can also be an independently generated electromagnetic pulse (Figure 9.3.3).

9.3.2.2 **Single-Photon Counting Technique**

Time-correlated single-photon counting (TCSPC) is based on the detection of single photons of a periodical light signal, the measurement of the detection times of the individual photons, and the reconstruction of the waveform from the individual time measurements [21, 22]. TCSPC method generates a histogram that represents the fluorescence lifetime. This is an efficient process because it counts photons and records arrival time in picoseconds, which directly represents the fluorescent decay. Time to amplifier converter (TAC) is used with a multichannel analyzer (MCA) to perform TCSPC. The TAC produces an electronic pulse with a height that is proportional to the time difference between the start pulse triggered by the excitation pulse and the stop pulse from the detector. The MCA receives the

electronic pulse from the TAC and converts the voltage into a channel address number of a storage memory. A histogram, which corresponds to the decay curves, is built up in the MCA with increasing numbers of events. The counting rate should be smaller than ~1%, so that the probability of a simultaneous arrival of two photons is negligible (<0.01%). Thus, a light source with a high repetition rate, for example, a mode-locked laser is required. The time resolution of this technique is determined by the jitter of the electric circuit, not by the width of the electric signal from the photosensors. Therefore, time resolution of tens of picoseconds can be achieved with a specially designed PMT. TAC is used for repetitive events and for single-photon counting. The time resolution with this system is ~10 ps.

The principle of the TCPSC technique is quite complicated; however, it is frequently used as it has several remarkable benefits

- The time resolution of TCSPC is limited by the transit time spread, not by the width of the output pulse of the detector. With fast MCP PMTs, an instrument response width of less than 30 ps is achieved.
- TCSPC has a near-perfect counting efficiency and therefore achieves optimum signal-to-noise ratio for a given number of detected photons.
- TCSPC is able to record the signals from several detectors simultaneously.
- TCSPC can be combined with a fast scanning technique and therefore be used as a high-resolution high-efficiency lifetime imaging (FLIM) technique in confocal and two-photon laser scanning microscopes.
- TCSPC is able to acquire fluorescence lifetime and fluorescence correlation data simultaneously [23].
- State-of-the-art TCSPC devices achieve count rates in the MHz range and acquisition times down to a few milliseconds.

9.3.2.3 **TRPL Imaging Technique**

The imaging of ultrafast photoluminescence or slower processes (fluorescence, phosphorescence) can readily be carried out with special optoelectronic equipment. The technique allows one to record simultaneously the intensity and the spectral and the temporal responses of fluorescence. A streak camera is widely used in time-resolved spectroscopy, because it enables us to obtain temporal and spectral information simultaneously. A schematic diagram of the streak camera is given in Figure 9.3.4. It should be pointed out that no other device devoted to the direct detection of light has better temporal resolution than a streak camera. The device can be considered as a time–space converter.

A spectrometer is usually installed before the streak camera in order to disperse the incoming light horizontally. The spectrally dispersed light impinges on a photocathode from which photoelectrons are emitted. The electrons are accelerated and temporally dispersed by the deflection electrodes subjected to a rapidly changing sweep voltage in the vertical direction. Then, the spectrally and temporally dispersed electrons hit a multichannel plate, which multiplies electrons while keeping their spatial distribution. The multiplied electrons irradiate a phosphor screen on which a so-called streak image appears. The image is recorded with a CCD camera.

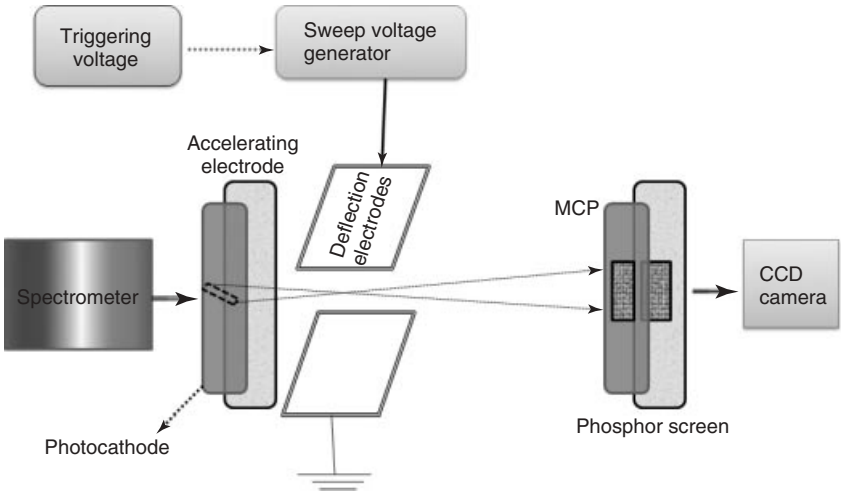

Figure 9.3.4 Schematic diagram of a streak camera.

Synchroscan streak cameras used for the mode-locked lasers with high repetition rates of ~100 MHz achieve picosecond time resolution.

9.3.2.4 Nonlinear Optical Techniques

9.3.2.4.1 Kerr Gate Technique

An extension of the optical gating technique is to use a "Kerr gate," which allows the optical signal to be collected before the (slower) fluorescence signal overwhelms it. Optical Kerr shutters utilize the optical Kerr effect in which a Kerr active medium is used as an optical gate (Figure 9.3.5).

In this method, a strong laser pulse induces birefringence in the Kerr medium, so that the plane of the polarization of the incident light determined by a polarizer P1 is rotated. Thus the incident light, normally blocked by a crossed polarizer P2, can pass through the P2. This configuration is inserted between the collection lenses and the spectrometer. The time-resolved spectrum is then obtained by changing

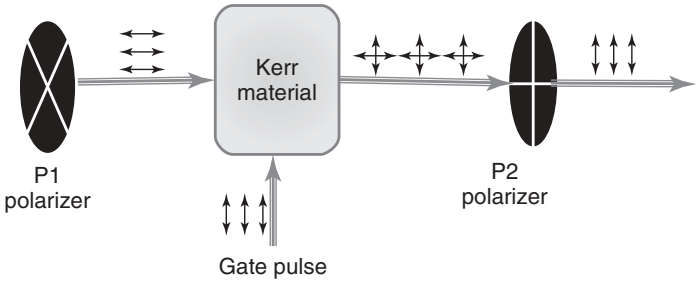

Figure 9.3.5 Principle of Kerr shutter.

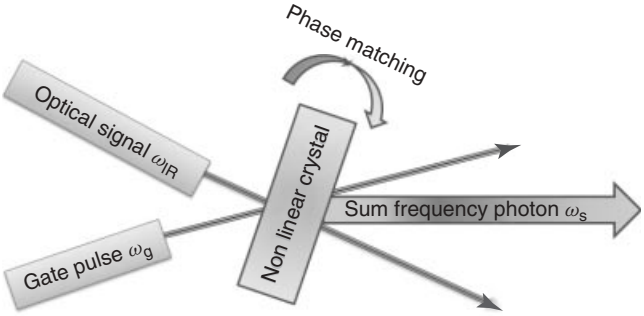

Figure 9.3.6 Schematic diagram of upconversion time-resolved spectroscopy.

the delay between the gate and incident pulses. Time resolution of approximately subpicosecond is possible.

9.3.2.4.2 Upconversion Technique

Upconversion (or optical mixing) is one of the most widely utilized methods for femtosecond time-resolved measurements [24]. With the advent of improved versions of the Ti:sapphire laser, the reliability of such experiments increases. Upconversion spectroscopy is based on sum frequency generation (SFG), which is used to generate higher frequency from the lower frequency. The upconverted photon ωs from IR optical signal ω_{IR} is emitted when the gating laser pulse ω_g irradiates the nonlinear crystal, shown in Figure 9.3.6. The spontaneous emission is mixed with another femtosecond pulse (gate) in a nonlinear crystal to generate the sum frequency of the gate and optical signal. The intensity of the generated signal is proportional to the intensity of the optical signal that is temporally overlapped with the gate pulse. Therefore, by measuring the upconverted signal while changing the delay time between the pump and the gate pulses, we can obtain a replica of the time-resolved emission. A combination of the pump pulse and the nonlinear crystal acts as an optical gate similar to the boxcar integrator. By sweeping the delay time of the pump pulse, a temporal profile of the luminescence is obtained. A time-resolved spectrum is obtained by scanning the crystal angle (and monochromator) for the phase-matching condition. The time resolution of ~100 fs is possible.

9.3.3 Case Study of ZnO

Despite the commercial success of the III–V gallium nitride (GaN) material system, interest in the II–VI semiconductor zinc oxide (ZnO) was renewed in the late 1990s when room temperature, optically pumped lasing was demonstrated for ZnO thin films [25–29]. Zinc oxide is recognized as a promising material for advanced photonics because of its wide bandgap (3.37 eV) and high exciton binding energy of 60 meV. The bulk exciton's binding energy of ZnO (60 meV) is much

higher than that of GaN (24 meV) and ZnSe (20 meV) that are close to kT at room temperature (26 meV), which is extensively used for the development of room temperature optoelectronic devices in the short wavelength range (green, blue, and UV), information storage and sensors [30–33]. The following are applications of optoelectronics: as blue-color-light-emitting phosphors [30], as nanorod UV light emitters [31], as fluorescence labels in medicine and biology, in controlling units as UV photodetectors and as high-flame detectors [32], as nanosensors of various gases, and also in the cosmetic industry, as a component of sun screens, are envisioned [33]. The high exciton binding energy of ZnO would allow excitonic transitions even at room temperature, which could mean high radiative recombination efficiency for spontaneous emission as well as a lower threshold voltage for laser emission. Studies have been carried out to fine-tune the properties of ZnO and to adopt it for different applications; for example, the bandgap of ZnO is modified to use as UV detectors and emitters. Recently, long lasting afterglow has been reported in ZnO nanocrystals, which is caused by the spin-dependent tunneling recombination and can last for a very long time (several hours) after switching off the ultraviolet (UV) light excitation [34]. Considering the vast commercial application in the field of display devices, biomedical, and others, it is necessary to standardize the ZnO samples using the precise TRPL technique for the quality control of the final product. In the following section, a brief about ZnO photoluminescence and a study using this technique are mentioned.

9.3.3.1 Origin of ZnO Photoluminescence

Nanometer-sized particles have very different physical and chemical properties from bulk materials; consequently, the optical behavior of ZnO is entirely different compared to its bulk counterparts [35]. The observed variation is not only due to increased surface area but also due to the changes of surface properties such as surface defects, adsorbed impurities etc. When the crystallite dimension of a semiconductor particle falls below a critical radius of approximately 50 nm, the charge carriers appear to behave quantum mechanically like simple particles in a box. This confinement produces a quantization of discrete electronic states and increases the effective bandgap of the semiconductor [36]. As a result, the band edges shift to yield larger redox potentials. The solvent reorganization free energy for charge transfer to a substrate, however, remains unchanged. The increased driving force resulting from the increased redox potential and the unchanged solvent reorganization free energy in size-quantized systems are expected to increase the rate constant of charge transfer and may result increased photoefficiencies of systems in which the rate-limiting step is charge transfer.

The optical and electronic properties of semiconductors can be further tuned by varying the size of the particles in the range below 10 nm. There is a great variety of the ZnO nanostructure morphologies [37] that has already been demonstrated, such as nanowires [38–40], nanoribbons [41], nanorods [42–44], tetrapod nanowires [45], microtubes [46], nanoneedles [47], nanohelixes, nanorings [48], and dendritic nanowire arrays [49].

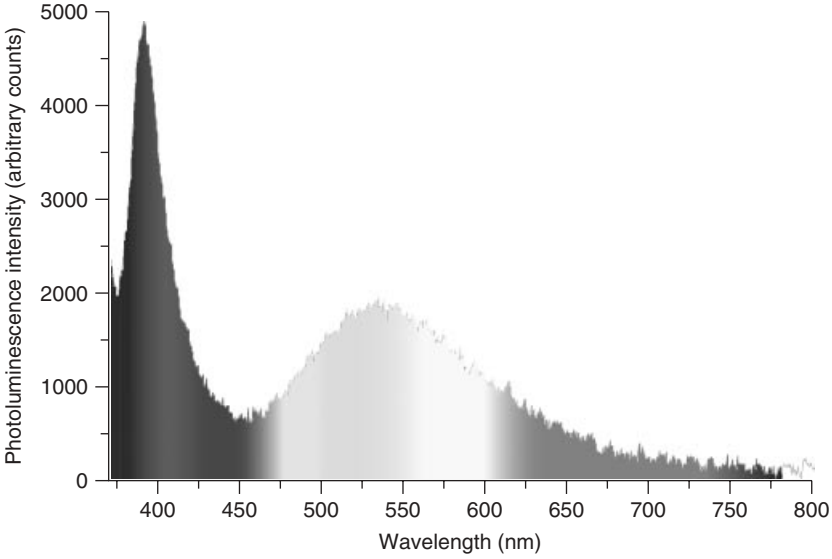

Figure 9.3.7 Typical photoluminescence spectrum of rod-shaped ZnO nanophosphor on excitation with 355 nm laser radiation.

Despite the myriad of potential applications of ZnO nanomaterials, several perplexing problems are yet to be solved, which evoked research among the scientists. One of the most discussed problems, still a matter of debate, is the chemical and structural origins of the visible luminescence from pure ZnO crystal. In general, photoluminescence spectra of ZnO crystals contain a sharp UV emission band (3.3 eV at 295 K) and a broad band in visible region (centered at ~2.5 eV) due to defects and/or impurities (Figure 9.3.7). In bulk ZnO and in thin films of good quality, the intensity of visible emission is of several orders of magnitude weaker than that of the band edge emission [50–53]. For ZnO nanostructures, however, the intensity of the defect emission can be much stronger. The most accepted explanation [54] of the defect emission is the recombination of electrons trapped at singly ionized oxygen vacancies with valence band holes. One other possible explanation [55] in literature is the recombining of electrons in the conduction band and/or shallow donor states with holes, which have been trapped at oxygen vacancies. As a detailed description about the origin of defect is beyond the scope of the chapter, hence only a brief introduction is given here: the crystal structure of ZnO is a relatively open structure, with a hexagonal close-packed lattice where Zn atoms occupy half of the tetrahedral sites, while all the octahedral sites are empty. This facilitates plenty of sites for ZnO to accommodate intrinsic (namely Zn interstitials) defects and extrinsic dopants [56]. There could be a number of intrinsic defects with different ionization energies. The Kröger Vink notation uses: i = interstitial site, Zn = zinc, O = oxygen, and V = vacancy. The terms indicate the atomic sites, and superscripted terms indicate charges, where a dot indicates positive charge, a prime the negative charge, and a cross zero charge, with the

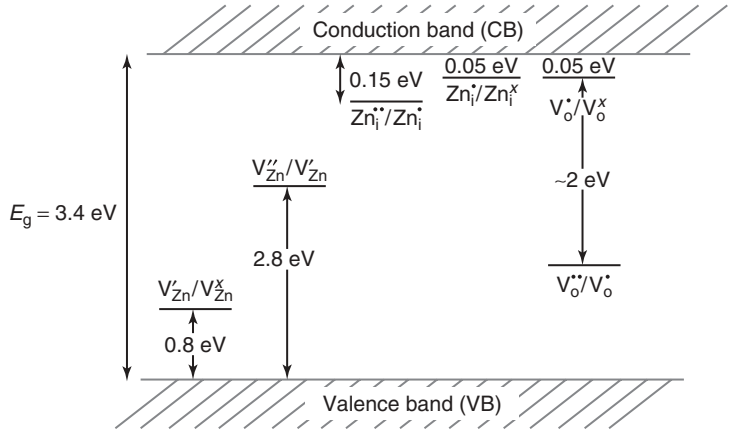

Figure 9.3.8 Energy levels of native defects in ZnO. The donor defects are $Zn_i^{\bullet\bullet}$, $Zn_i^{\bullet}$, Zn_i^{x}, $V_o^{\bullet\bullet}$, $V_o^{\bullet}$, and V_o, and the acceptor defects are V_{Zn}'' and V_{Zn}. (Source: Figure from Book Ref. [59].)

charges in proportion to the number of symbols. A number of defect states within the bandgap of ZnO are clearly visible. The observed defects are $Zn_i^{\bullet\bullet}$, $Zn_i^{\bullet}$, Zn_i^{x}, $V_o^{\bullet\bullet}$, $V_o^{\bullet}$, and V_o, and the acceptor defects are V_{Zn}'', V_{Zn}' (Figure 9.3.8). These defects are a function of dopant, concentration, shape, and structure of nanomaterials. The defect ionization energies vary from ~0.05–2.8 eV [57]. Zn interstitials and oxygen vacancies are known to be the predominant ionic defect types. However, which defect dominates in native, undoped ZnO is still a matter of great controversy [58].

Shalish *et al.* [60] demonstrated that the intensity of defect emission in an array of ZnO nanowires was directly proportional to the average surface-to-volume ratio of wire. Measurements of the polarization of band edge versus defect emission [61] and studies involving surfactant treatments in ZnO nanostructures [62, 63] also indicate that the visible emission originates from the surfaces of these materials.

The high exciton-binding energy at room temperature evoked the possibility of stimulated emission at room temperature, which has a lower threshold than electron–hole plasma recombination. However, as a matter of fact, still no report on electrically pumped lasing is reported, whereas optically pumped lasing and amplified spontaneous emission are available in several reports [28, 64, 65]. Amplified spontaneous emission was reported for a self-organized network of ZnO fibers [41], while lasing has been reported in nanowires [29, 66], tetrapods, [40, 67], and nanoribbons/combs [64].

Owing to these perplexing problems, the study of stimulated emission [38, 39, 42, 68] and temperature-dependent photoluminescence [69, 70] in ZnO is of great interest. Typically, the stimulated emission decay time is much faster than that of the spontaneous emission, so that it may be below the detection limit of few TRPL systems [71]. Emissions in the exciton–exciton (EE) and exciton–hole Plasma (EHP) regime exhibit different behaviors with time [45, 72]. The comparison

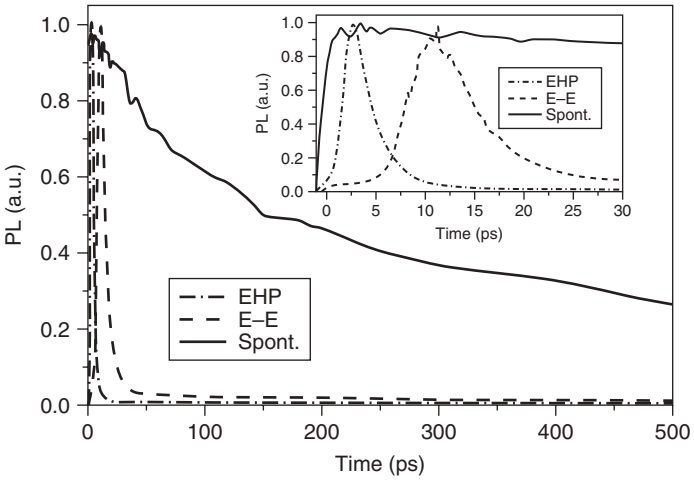

Figure 9.3.9 The radiative decay curves of the exciton–exciton (EE), exciton–hole plasma (EHP), and spontaneous (spon.). A magnified portion of −1 to 30 ps is given in the inset [73]. PL, photoluminescence.

between the decay curves of the spontaneous emission, EE, and EHP emissions from highly faceted rods is shown in Figure 9.3.9.

It is clear that although both types of stimulated emission have a shorter decay time compared to spontaneous emission, there are obvious differences in their temporal evolution. The EHP emission peak exhibits some shifting with time, which was established by direct measurements of the lasing spectra [45, 72–74] as well as by measuring transient profiles of the lasing dynamics as a function of wavelength [39]. EHP emission has a small rise time (1–2 ps) ascribed to the thermalization of the hot carriers [73, 75], and the decay time is of a few picoseconds [64, 72, 75]. The decay time of the lasing could be longer in case of long cavity length, lower losses at end facets, and lower defect concentrations [64]. In contrast to EHP emission, stimulated emission in the EE regime exhibits a long rise time as a longer time would be needed to achieve a high concentration of excitons in the excited state [72, 76]. However, the decay time of EHP emission and the EE emission is comparable [72, 77]. With respect to the evolution of the lasing spectra and any peak shifts in the EE regime, some spectral shifts of the peaks can be observed with time [78], but it is difficult to analyze the data because the measurements have been performed on an ensemble of the nanostructures.

The occurrence of stimulated emission in ZnO nanostructures at comparably lower threshold pump power density attracts attention [38, 39]. The high exciton binding energy of ZnO facilitates the lasing at a comparably lower threshold power density and due to that the excitation of the excitons is less probable, that is, low energy loss through nonradiative process [79]. The lasing in ZnO nanostructures could be achieved by two different methods: first, lasing from a cavity formed between two facets of individual ZnO nanostructures, and second, lasing due to coherent scattering in random media [80].

9.3.3.2 Time-Resolved Spectroscopy of ZnO

Similar to the confinement effect observed in absorption and emission spectra, confinement also affects the radiative recombination of excitons, as the exciton–photon coupling in nanosize (1–10 nm) is particularly strong and the exciton radiative recombination rate drastically varies with the size [12]. The size-dependent radiative lifetime of exciton in ZnO nanocrystals were calculated by Fonoberov and Balandin [81, 82]. The effect of the geometrical confinement of the ZnO quantum dots inside the SiO_x matrix on the exciton radiative lifetime is discussed by Zhang *et al.* [83]. They have observed that the confinement reduces the exciton radiative lifetime. The reduction of the exciton radiative lifetime is discussed in terms of exciton superradiance. Superradiance is the cooperative radiative decay of an initially inverted assembly of quantum oscillators. It generates from systems smaller then incident wavelength and when all oscillator strength is cooperated in one collective superradiant excited state. This leads to an enhancement of the optical transition oscillator strength and thus to a shortening of the excitation radiative lifetime. The effect of exciton superradiance has also been studied in semiconductor nanocrystals [84] and several other geometrically confined systems. Kayanuma [85] theoretically studied the quantum-size effects of Wannier excitons in semiconductor nanocrystals and found that the exciton radiative lifetime in the weak confinement region decreases rapidly with the size of the nanocrystal as a result of exciton coherence effect, in other words, the exciton superradiance. The decay time of luminescence is the subject of photon–matter interactions. These interactions include the radiative decay of the exciton polariton and various nonradiative processes, such as leak by deep-level traps, low-lying surface states, and multiphonon scattering. The exciton polariton luminescence is, however, quite sensitive to the concentration of defects and structural factors of the nanostructures, and it is not easy to separate the radiative recombination and nonradiative processes.

Size dependence of the TRPL has been investigated for the ZnO nanorods fabricated with catalyst-free metal–organic chemical vapor deposition [86]. The radiative recombination rate decreases as the length of the nanorods increases monotonically in the range of 150–600 nm. The variation in the decay time with the length of the rods is given in Table 9.3.1 and Figure 9.3.10. The coupling of the excitons with the electromagnetic wave; that is, the exciton–polariton effect is invoked to account for the results. This relation between the size of nanoparticles and radiative decay time appears when the size is comparable to the wavelength of the excitation light.

The ZnO tetrapods shows exceptional optical properties, that is, intense UV emission, no defect emission, and a photoluminescence lifetime in the range of tens of nanoseconds at room temperature, which is strongly dependent on the growth temperature. For individual tetrapods, the photoluminescence lifetimes were significantly longer than the ZnO, including nanorods ($\tau_1 = 190$ ps, $\tau_2 = 1.4$ ns) [87], epilayers ($\tau = 3.8$ ns) [88], and single crystals ($\tau_1 = 1$ ns, $\tau_2 = 14$ ns) [89]. ZnO single crystals exhibited biexponential decay, while the tetrapod structure exhibited single exponential or biexponential decay. In biexponential decay, the fast decay constant is typically attributed to nonradiative recombination, while the slow

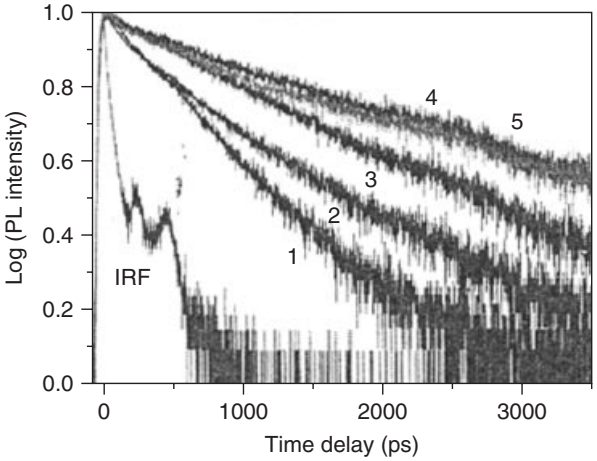

Figure 9.3.10 Decay curves of the samples (1–5 given in Table 9.3.1). Instrumental response function of the apparatus is also shown in Ref. [86]. PL, photoluminescence.

Table 9.3.1 Sizes of the ZnO nanorods and the time constants from the two exponential fits.

Sample	Diameter	Length (nm)	τ_1 (ps)	τ_2 (ps)
1	29	159	61 (44%)	291 (56%)
2	40	309	52 (61%)	447 (39%)
3	35	479	138 (42%)	786 (58%)
4	36	582	190 (37%)	1395 (63%)
5	40	1100	167 (51%)	1328 (49%)

Uncertainties in the diameter and length of the ZnO nanorods are 5 and 20 nm, respectively [86].

decay constant is attributed to the radiative lifetime of the free exciton [90]. If the recombination process was dominated by nonradiative channels, the lifetime would decrease with increasing temperature, since the nonradiative channels would play a more important role with temperature. These tetrapods exhibited an increase in the photoluminescence decay time with increasing temperature, indicating that the radiative recombination is the dominant recombination process.

Owing momentum conservation, usually all excitons cannot couple with the incident radiation field to yield photons. Theoretically, only those excitons at $k = 0$ can recombine radiatively; however, in practice, not only excitons at $k = 0$ contribute to the radiative recombination. It is observed that the homogeneous exciton linewidth has a certain spectral width ΔE at finite temperature. Actually, excitons with kinetic energy smaller than ΔE, the spectral linewidth of the transition, could recombine radiatively [91]. Exciton radiative lifetime is a function of temperature as the exciton redistribution occurs at elevated temperature. Effect of temperature on

exciton radiative lifetime depends on dimensionality of the investigated structures and the ratio between homogeneous free exciton linewidth and thermal energy kT. If the exciton linewidth is less than the thermal energy, the radiative lifetime has been shown to change as $\tau_r = \tau_0/r(T)$ where τ_0 is the radiative lifetime at $T = 0$ and $r(T)$ is a fraction of free exitons with kinetic energy smaller than kT. On increasing temperature of the system, the average kinetic energy of the free excitons increased, hence the ratio $r(T)$ of excitons decreases. Therefore, the exciton radiative lifetime will increase with temperature.

For three-dimensional systems such as the studied ZnO tetrapods and assuming a Maxwell–Boltzmann distribution, *r(T)* is roughly proportional to $T^{-3/2}$ and is given by

$$r(T) = \frac{2}{\sqrt{\pi}} \int_0^{\Gamma/kT} \sqrt{E} \exp(-E)\, dE \tag{9.3.15}$$

where E denotes the free exciton energy. This results in the characteristic $\tau_r \alpha\ T^{3/2}$ dependence, often reported in bulk semiconductors [92]. In the opposite case when thermal energy is less than exciton linewidth, however, τ_r is proportional to the homogenous linewidth and, therefore, changes with temperature. The exciton linewidth $\Gamma(T)$, dependence is mainly determined by interactions of excitons with acoustic and optical phonons as follows [91]

$$\Gamma(T) = \Gamma_0 + \gamma_a T + \frac{\Gamma_{LO}}{\left[\exp\left(\hbar\omega_{LO}/kT\right) - 1\right]} \tag{9.3.16}$$

Here, $\hbar_{\omega LO}$ is the energy of a LO phonon, Γ_0 is the zero temperature broadening parameter, γ_a is the coupling strength of an exciton–acoustic phonon interaction, and Γ_{LO} is a parameter describing exciton–LO–phonon interaction.

In the case of ZnO nanorods, the exciton radiative lifetime increases with temperature (T^2). Furthermore, the spectral linewidth of the photoluminescence of the ZnO nanorods also increases with temperature as T^2, suggesting a linear dependence of exciton radiative lifetime on the spectral line width. A plot between the exciton radiative lifetime and the spectral line width is given in Figure 9.3.11, which shows a linear relationship between the spectral line width and radiative lifetime. Similar behavior is also reported by Feldmann *et al.* in GaAs quantum wells.

The physics behind is that the $k = 0$ oscillator strength is shared equally among all the states within the spectral line width ΔE [91]. That means the exciton radiative recombination rate is not solely determined by the exciton oscillator strength but depends on the coherence extension of an exciton, which decreases with temperature due to scattering by phonons, defects, or impurities.

Emission lifetime is also a function of excitation energies. The picosecond TRPL measurements of star-shaped ZnO nanostructures show a biexponential decay behavior, which is strongly dependent on the excitation intensity; the slow decay term decreased faster than the fast decay term as the excitation intensity increased and the emission decays were dominated by the fast one [94]. It was also reported that the emission decays decreased superlinearly before the appearance of the

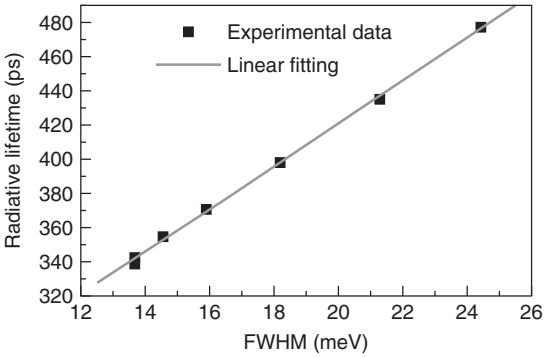

Figure 9.3.11 Spectral linewidth dependence of the exciton radiative lifetime. The solid squares stand for experimental data. The linear fit of the experimental data is given in Ref. [93]. FWHM, full width at half maximum.

stimulated emission (SE). This behavior may be used to deduce the threshold of SE or lasing. Wilkinson *et al.* [95] reported that a free exciton in ZnO single crystal has a lifetime of 403 ps at room temperature, and the lifetime of trapped carriers is approximated to 3.8 ns. Bauer *et al.* [96] reported that a direct radiative recombination of excitons can take place with a time constant of 12 ps in ZnO nanocrystalline thin films. Moreover, Guo *et al.* [97] reported that the time constant for the capture of free excitons at the band-tail states is on the order of 30 ps, and a slower decay term of 100–400 ps is associated with radiative recombination of free or localized excitons. In fact, different lifetime behaviors have been observed for ZnO with a fast time constant ranging from ~10 to several tens of picoseconds and a slow term ranging from several hundreds of picoseconds to nearly 20 ns, and the reported time decay is usually smaller than 100 ps when a stimulated emission or a lasing action took place in ZnO nanocrystals [98, 99].

Study of ultrafast carrier dynamics in exciton–exciton scattering and electron–hole plasma regimes of ZnO nanoneedles shows very fast decay time (1 ps) of the photoluminescence. Even though no structure is detected in the time-integrated spectra of the electron hole plasma emission, the TRPL photoluminescence reveals the coexistence of the excitons and free carriers. The shortest decay time previously reported for ZnO lasing is 3 ps [100]. The similar rise time of 1 ps for the electron–hole plasma regime is reported in other cases too [101]. The decay curve of the stimulated emission in the exciton–exciton regime shows a similar rise time and no significant delay time, unlike ZnO tetrapod nanostructures [44] and nanoribbons and nanowires [40]. Longer delay time until the onset of exciton–exciton lasing was previously attributed to the longer time for the weak exciton–exciton interaction to produce sufficient scattering events [40].

Ozgur *et al.* [50] investigated the effect of annealing and stimulated emission on carrier dynamics in RF-sputtered ZnO thin films at room temperature and at 85 K using TRPL spectroscopy. The exciton densities were kept slightly below the threshold I_{th}(~30 μJ cm^{-2}) to measure the spontaneous emission decay times,

while high excitation densities ($\sim$200 μJ cm^{-2}) were used to observe the recombination dynamics under the influence of stimulated emission, single exponential decay fit revealed the spontaneous recombination times as 74, 59, and 30 ps for the samples annealed at 1000, 950, and 800 °C, respectively. Increment in the decay times with annealing temperature suggests a reduction in the density of nonradiative recombination centers. As expected, the stimulated-emission-induced recombination occurs very fast (<30 ps). The decay curve for above excitation threshold also show a much weaker and slower decaying component visible after the stimulated emission is over ($\sim$55 ps) with the characteristic decay times of the spontaneous recombination.

Reynolds *et al.* [102] measured the recombination lifetime of the allowed (Λ_5) and forbidden-free excitons (Λ_6 allowed by induced strain) at 2 K in a strained single crystal ZnO grown by the hydrothermal method as 259 and 245 ps, respectively. The lifetime of the Λ_5 exciton was slightly higher, 322 ps, for an unstrained sample. They noted that free exciton lifetimes are determined not only by the radiative decay but also by the nonradiative decay and capture processes leading to bound excitons. In general, pure ZnO shows n-type conductivity, while the Zn interstitials (Zn_i) and/or Oxygen vacancies (V_O) are the sources of free electrons. However, the role of neutral and negatively charged defects has not been clarified yet, although their presence has been pointed out [103]. In case of semiconductor positrons, the annihilation technique is mostly used for the study of neutral/charged defects [104]. In case of ZnO, Zn vacancy (V_{Zn}) is one of the most probable candidates. Because the momentum distribution of electrons in such defects differs from that in bulk materials, the annihilating positron–electron pairs show Doppler broadening for the 511 keV annihilation γ-rays. The resultant spectrum is characterized by the S parameter, which mainly reflects the fraction of annihilation of positron–electron pairs with a low momentum distribution. It was reported that the epitaxial ZnO layers exhibited shorter carrier lifetimes because of the higher defect densities compared to the bulk samples. Detailed study was done by Koida *et al.* [105]. They studied the influences of point defects on the nonradiative processes in ZnO using steady-state and time-resolved photoluminescence spectroscopy, making a connection with the results of positron annihilation measurement in bulk and epitaxial ZnO layers. The single crystal sample showed biexponential behavior with decay constants of 0.97 and 14 ns, which were suggested to represent the free exciton lifetime and the free carrier lifetime including trapping and emission processes. Pure ZnO epitaxial films were grown by combinatorial laser molecular-beam epitaxy [106]. The single exponential decay time, which is mainly governed by nonradiative process, increased from 46 to 110 ps with increasing growth temperature from 570 to 800 °C. Although homoepitaxial film exhibits the shortest decay time (36 ps) in spite of the smallest number of point defects among the epilayers, the relation between the photoluminescence decay time and the point defect density is ambiguous. It could be concluded that the nonradiative process was induced by certain defect species, which occurs because of the presence of Zn vacancies such as vacancy complexes.

Decay curve analysis of high-quality ZnO epitaxial layers grown on sapphire by low-pressure metal organic vapor-phase epitaxy was investigated by Jung *et al*. [107]. They reported biexponential decay behavior of ZnO and the decay times extracted was 180 ps and 1 ns, due to the nonradiative and radiative excitonic recombination times, respectively, consistent with the measurements of Teke *et al*. [108] and Koida *et al*. [105] in bulk ZnO samples.

9.3.4
Concluding Remarks

The advent of lasers 50 years ago has put the spectroscopic techniques on a very high pedestal. Technology has succeeded in gaining control over the pulse width of the laser and achieved fascinating autosecond pulse width, which may help to monitor even the shortest ever event at the atomic level. One of the applications of lasers is the understanding of the relaxation dynamics of the excited species, which is only possible when one has ultrashort laser pulses. In this chapter, a brief illustration of the importance of TRPL was presented especially in terms of nanomaterials. TRPL gives a detailed insight into the dynamics of excited species, and the many aspects of other processes that are highly in demand for the quality control of nanomaterial-based products. One such important nanomaterial, ZnO, which is gaining importance due to its commercial aspects, was also discussed.

References

1. Miller, R.C., Kleinman, D.A., Tsang, W.T., and Gossard, A.C. (1981) *Phys. Rev. B*, **24**, 1134.
2. Rossetti, R., Nakahara, S., and Brus, L.E. (1983) *J. Chem. Phys.*, **79**, 1086.
3. Brus, L.E. (1984) *J. Chem. Phys.*, **80**, 4403.
4. Misawa, K., Yao, H., Hayashi, T., and Kobayashi, T. (1991) *J. Chem. Phys.*, **94**, 4131.
5. Guo, L., Yang, S., Yang, C., Yu, P., Wang, J., Ge, W., and Wong, G.K.L. (2000) *Appl. Phys. Lett.*, **76**, 2901.
6. Morkoç, H. and Özgür, Ü. (2009) *Zinc Oxide: Fundamentals, Materials and Device Technology*, Wiley-VCH Verlag GmbH.
7. Gilliland, G.D. (1997) *Mater. Sci. Eng.*, **18**, 99–400.
8. Yacobi, B.G. and Holt, D.B. (1990) *Cathodoluminescence Microscopy of Inorganic Solids*, 1st edn, Plenum Press, New York.
9. Glinka, Y.D., Shahbazyan, T.V., Peraki, I.E., Talk, N.H., Liu, X.Y., Sasaki, Y., and Furdyna, J.K. (2002) *Appl. Phys. Lett.*, **81**, 3717.
10. Mikhailovsky, A.A., Malko, A.V., Hollingsworth, J.A., Bawendi, M.G., and Klimov, V.I. (2002) *Appl. Phys. Lett.*, **80**, 2380.
11. Klimov, V.I., Mikhailovsky, A.A., Xu, S., Malko, A., Hollingsworth, J.A., Leatherdale, C.A., Eisler, H.J., and Bawendi, M.G. (2000) *Science*, **290**, 314.
12. Gil, B. and Kavokin, A.V. (2002) *Appl. Phys. Lett*, **81**, 748.
13. Norris, D.J., Efros, A.L., Rosen, M., and Bawendi, M.G. (1996) *Phys. Rev. B*, **53**, 16347.
14. Colvin, V.L., Alivisatos, A.P., and Shank, C.V. (1994) *Phys. Rev. B*, **49**, 14435.
15. Chichibu, S., Azuhata, T., Sota, T., Amano, H., and Akasaki, I. (1997) *Appl. Phys. Lett.*, **70**, 2085.

16. Shikanai, A., Azuhata, T., Sota, T., Chichibu, S., Kuramata, A., Horina, K., and Nakamura, S. (1997) *J. Appl. Phys.*, **81**, 417.
17. Foreman, J.V., Li, J., Peng, H., Choi, S., Everitt, H.O., and Liu, J. (2006) *Nano Lett.*, **6**, 1126.
18. Reynolds, D.C., Look, D.C., Jogai, B., Hoelscher, J.E., Sherriff, R.E., and Molnar, R.J. (2000) *J. Appl. Phys.*, **88**, 1460.
19. Bergman, J.P., Holtz, P.O., Monemar, B., Sun Da Ram, M., Merz, J.L., and Gossard, A.C. (1991) *Phys. Rev. B*, **43**, 4765.
20. Lefebvre, P., Allegre, J., and Mathieu, H. (1999) *Mater. Sci. Eng. B*, **59**, 307.
21. O'Connor, D.V. and Phillips, D. (1984) *Time Correlated Single Photon Counting*, Academic Press, London.
22. Becker, W., Bergmann, A., Biskup, C., Kelbauskas, L., Zimmer, T., Klöcker, N., and Benndorf, K. (2003) *Proc. SPIE*, **4963**, 1–10.
23. Ballew, R.M. and Demas, J.N. (1989) *Anal. Chem.*, **61**, 30–33.
24. Mahr, H. and Hirsch, M.D. (1975) *Opt. Commun.*, **13**, 96.
25. Bagnall, D.M., Chen, Y.F., Zhu, Z., Yao, T., Shen, M.Y., and Goto, T. (1998) *Appl. Phys. Lett.*, **73**, 1038–1040.
26. Tang, Z.K., Wong, G.K.L., Yu, P., Kawasaki, M., Ohtomo, A., Koinuma, H., and Segawa, Y. (1998) *Appl. Phys. Lett.*, **72**, 3270–3272.
27. Zu, P., Tang, Z.K., Wong, G.K.L., Kawasaki, M., Ohtomo, A., Koinuma, H., and Segawa, Y. (1997) *Solid State Commun.*, **103**, 459.
28. Bagnall, D.M., Chen, Y.F., Zhu, Z., Yao, T., Koyama, S., Shen, M.Y., and Goto, T. (1997) *Appl. Phys. Lett.*, **70**, 2230–2232.
29. Reynolds, D.C., Look, D.C., and Jogai, B. (1996) *Solid State Commun.*, **99**, 873.
30. Hayashi, H., Ishizaka, A., Haemori, M., and Koinuma, H. (2003) *Appl. Phys. Lett.*, **82**, 1365.
31. Ng, H.T., Chen, B., Li, J., Han, J., Meyyappan, M., Wu, J., Li, S.X., and Haller, E.E. (2003) *Appl. Phys. Lett.*, **82**, 2023.
32. Sharma, P., Sreenivas, K., and Rao, K.V. (2003) *J. Appl. Phys.*, **93**, 3963.
33. Look, D.C. (2001) *Mater. Sci. Eng. B*, **80**, 383.
34. (a) Baranov, P.G., Romanov, N.G., Tolmachev, D.O., Orlinskii, S.B., Schmidt, J., de Mello Donega, C., and Meijerink, A. (2006) *JETP Lett.*, **84**, 400; (b) Full Text via CrossRef | View Record in Scopus | Cited By in Scopus (1) Baranov, P.G., Romanov, N.G., Tolmachev, D.O., Orlinskii, S.B., Schmidt, J., de Mello Donega, C., and Meijerink, A. (2006) *JETP Lett.*, **84**, 400.
35. Singh, S., Thiyagarajan, P., Mohan Kant, K., Anita, D., Thirupathiah, S., Rama, N., Tiwari, B., Kottaisamy M., and Ramachandra Rao, M.S. (2007) *J. Phys. D: Appl. Phys.*, **40**, 6312–6327.
36. Jung, K.Y., Kang, Y.C., and Park, S.B. (1997) *J. Mater. Sci. Lett.*, **22**, 1848.
37. Wang, Z.L. (2004) *Nanostruct. Zinc Oxide, Mater. Today*, **7**, 26–33.
38. Huang, M.H., Mao, S., Feick, H., Yan, H., Wu, Y., Kind, H., Weber, E., Russo, R., and Yang, P. (2001) *Science*, **292**, 1897.
39. Liu, C., Zapien, J.A., Yao, Y., Meng, X., Lee, C.S., Fan, S., Lifshitz, Y., and Lee, S.T. (2003) *Adv. Mater.*, **15**, 838.
40. Johnson, J.C., Yan, H., Yang, P., and Saykally, R.J. (2003) *J. Phys. Chem. B*, **107**, 8816.
41. Yan, H., Johnson, J., Law, M., He, R., Knutsen, K., McKinney, J.R., Pham, J., Saykally, R., and Yang, P. (2003) *Adv. Mater.*, **15**, 1907.
42. Yu, S.F., Yuen, C., Lau, S.P., Park, W.I., and Yi, G.-C. (2004) *Appl. Phys. Lett.*, **84**, 3241.
43. Choy, J.-H., Jang, E.-S., Won, J.-H., Chung, J.-H., Jang, D.-J., and Kim, Y.-W. (2003) *Adv. Mater.*, **15**, 1911.
44. Qiu, Z., Wong, K.S., Wu, M., Lin, W., and Xu, H. (2004) *Appl. Phys. Lett.*, **84**, 2739.
45. Leung, Y.H., Kwok, W.M., Djurisic, A.B., Phillips, D.L., and Chan, W.K. (2005) *Nanotechnology*, **16**, 579.
46. Sun, X.W., Yu, S.F., Xu, C.X., Yuen, C., Chen, B.J., and Li, S. (2003) *Jpn. J. Appl. Phys.*, **42**, L1229.

47. Kwok, W.M., Djurişiæ, A.B., Leung, Y.H., Chan, W.K., and Phillips, D.L. (2005) *Appl. Phys. Lett.*, **87**, 093108.
48. Kong, X.Y. and Wang, Z.L. (2003) *Nano Lett.*, **3**, 1625.
49. Yan, H., He, R., Johnson, J., Law, M., Saykally, R.J., and Yang, P. (2003) *J. Am. Chem. Soc.*, **125**, 4728.
50. Ozgur, U., Teke, A., Liu, C., Cho, S.J., Morkoc, H., and Everitt, H.O. (2004) *Appl. Phys. Lett.*, **84**, 3223–3225.
51. Wang, L. and Giles, N.C. (2003) *J. Appl. Phys.*, **94**, 973.
52. Leiter, F., Alves, H., Pfisterer, D., Romanov, N.G., Hofmann, D.M., and Meyer, B.K. (2003) *Phys. B*, **340–342**, 201.
53. Jung, S.W., Park, W.I., Cheong, H.D., Gyu-Chul, Y., Hyun, M.J., Hong, S., and Joo, T. (2002) *Appl. Phys. Lett.*, **80**, 1924–1926.
54. Vanheusden, K., Warren, W.L., Seager, C.H., Tallant, D.R., Voigt, J.A., and Gnade, B.E. (1996) *J. Appl. Phys.*, **79**, 7983.
55. van Dijken, A., Meulenkamp, E.A., Vanmaekelbergh, D., and Meijerink, A. (2000) *J. Phys. Chem. B*, **104**, 1715.
56. Mende, L.S. and Driscoll, J.L.M. (2007) *Mater. Today*, **10**, 40–48.
57. Han, J. *et al.* (2002) *J. Eur. Ceram. Soc.*, **22**, 49.
58. Hagemark, K.I. (1976) *J. Solid State Chem.*, **16**, 293.
59. Kröger, F.A. (1974) *The Chemistry of Imperfect Crystals*, 2nd edn, North Holland, Amsterdam, p. 73.
60. Shalish, I., Temkin, H., and Narayanamurti, V. (2004) *Phys. Rev. B*, **69**, 245401.
61. Hsu, N.E., Hung, W.K., and Chen, Y.F. (2004) *J. Appl. Phys.*, **96**, 4671.
62. Li, D., Leung, Y.H., Djurisic, A.B., Liu, Z.T., Xie, M.H., Shi, S.L., Xu, S.J., and Chan, W.K. (2004) *Appl. Phys. Lett.*, **85**, 1601–1603.
63. Djurisic, A.B., Leung, Y.H., Choy, W.C.H., Cheah, K.W., and Chan, W.K. (2004) *Appl. Phys. Lett.*, **84**, 2635–2637.
64. Song, J.K., Szarko, J.M., Leone, S.R., Li, S., and Zhao, Y. (2005) *J. Phys. Chem. B*, **109**, 15749.
65. Kwok, W.M., Leung, Y.H., Djurisic, A.B., Chan, W.K., and Phillips, D.L. (2005) *Appl. Phys. Lett.*, **87**, 093108.
66. Xu, C.X., Sun, X.W., Yuen, C., Yu, S.F., and Dong, Z.L. (2005) *Appl. Phys. Lett.*, **86**, 011118.
67. Sarko, J.M., Song, J.K., Blackledge, C.W., Swart, I., Leone, S.R., Li, S., and Zhao, Y. (2005) *Chem. Phys. Lett.*, **404**, 171.
68. Djurisic, A.B., Kwok, W.M., Leung, Y.H., Chan, W.K., and Phillips, D.L. (2005) *J. Phys. Chem. B*, **109**, 19228.
69. Kato, H., Sano, M., Miyamoto, K., Yao, T., Zhang, B.-P., Wakatsuki, K., and Segawa, Y. (2004) *Phys. Status Solidi B*, **241**, 2825.
70. Meyer, B.K., Alves, H., Hofmann, D.M., Kreigseis, W., Forster, D., Bertram, F., Christen, J., Hoffmann, A., Strasburg, M., Dworzak, M., Haboeck, U., and Rodina, A.V. (2004) *Phys. Status Solidi B*, **241**, 231.
71. Cao, L., Zou, B., Li, C., Zhang, Z., Xie, S., and Yang, G. (2004) *Europhys. Lett.*, **68**, 740.
72. Kwok, W.M., Leung, Y.H., Djurišić, A.B., Chan, W.K., and Phillips, D.L. (2005) *Appl. Phys. Lett.*, **87**, 093108.
73. Kwok, W.M., Djurisic, A.B., Leung, Y.H., Chan, W.K., Phillips, D.L., Chen, H.Y., Wu, C.L., Gwo, S., and Xie, M.H. (2005) *Chem. Phys. Lett.*, **412**, 141.
74. Takeda, J., Kurita, S., Chen, Y., and Yao, T. (2001) *Int. J. Mod. Phys. B*, **15**, 3669.
75. Yamamoto, A., Kido, T., Goto, T., Chen, Y., Yao, T., Kasuya, A., and Cryst, J. (2000) *Growth*, **214**, 308.
76. Johnson, J.C., Knutsen, K.P., Yan, H., Law, M., Zhang, Y., Yang, P., and Saykally, R.J. (2004) *Nano Lett.*, **4**, 197.
77. Kwok, W.M., Djurišića, A.B., Leung, Y.H., Chan, W.K., and Phillips, D.L. (2005) *Appl. Phys. Lett.*, **87**, 223111.
78. Djurišić, A.B., Kwok, W.M., Leung, Y.H., Chan, W.K., and Phillips, D.L. (2005) *J. Phys. Chem. B*, **109**, 19228.
79. Zhang, X.Q., Suemune, I., Kumano, H., Yao, Z.G., and Huang, S.H. (2008) *J. Lumin.*, **122–123**, 828.
80. Hsu, H.-C., Wu, C.-Y., and Hsieh, W.-F. (2005) *J. Appl. Phys.*, **97**, 064315.

81. Fonoberov, V.A. and Balandin, A.A. (2005) *Appl. Phys. Lett.*, **86**, 226101.

82. Fonoberov, V.A. and Balandin, A.A. (2004) *Appl. Phys. Lett.*, **85**, 5971.

83. Zhang, X.H., Chua, S.J., Yong, A.M., Chow, S.Y., Yang, H.Y., Lau, S.P., and Yu, S.F. (2006) *Appl. Phys. Lett.*, **88**, 221903.

84. Itoh, T., Furumiya, M., Ikehara, T., and Gourdon, C. (1990) *Solid State Commun.*, **73**, 271.

85. Kayanuma, Y. (1988) *Phys. Rev. B*, **38**, 9797.

86. Hong, S., Joo, T., Park, W., Ho Jun, Y., and Yi, G.C. II (2003) *Appl. Phys. Lett.*, **83**, 4157.

87. Hong, S., Joo, T., Park, W.I., Jun, Y.H., and Yi, G.-C. (2003) *Appl. Phys. Lett.*, **83**, 4157.

88. Chichibu, S.F., Onuma, T., Kubota, M., Uedono, A., Sota, T., Tsukazaki, A., Ohtomo, A., and Kawasaki, M. (2006) *J. Appl. Phys.*, **99**, 093505.

89. Koida, T., Uedono, A., Tsukazaki, A., Sota, T., Kawasaki, M., and Chichibu, S.F. (2004) *Phys. Status Solidi A*, **201**, 2841.

90. Ozgur, U., Alivov, Y.I., Liu, C., Teke, A., Reshchikov, M.A., Dogan, S., Avrutin, V., Cho, S.-J., and Morkoc, H. (2005) *J. Appl. Phys.*, **98**, 041301.

91. Feldmann, J., Peter, G., Göbel, E.O., Dawson, P., Moore, K., Foxon, C., and Elliott, R.J. (1987) *Phys. Rev. Lett.*, **59**, 2337.

92. p'tHooft, G.W., van der Poel, W.A.J.A., Molenkamp, L.W., and Foxon, C.T. (1987) *Phys. Rev. B*, **35**, 8281.

93. Zhang, X.H., Chua, S.J., Yong, A.M., Yang, H.Y., Lau, S.P., Yu, S.F., Sun, X.W., Miao, L., Tanemura, M., and Tanemura, S. (2007) *Appl. Phys. Lett.*, **90**, 013107.

94. Li, C.P., Guo, L., Wu, Z.Y., Ren, L.R., Ai, X.C., Zhang, J.P., Lv, Y.Z., Xu, H.B., and Yu, D.P. (2006) *Solid State Commun.*, **139**, 355–359.

95. Wilkinson, J., Ucer, K.B., and Williams, R.T. (2004) *Rad. Meas.*, **38**, 501.

96. Bauer, C., Boschloo, G., Mukhtar, E., and Hagfeldt, A. (2004) *Chem. Phys. Lett.*, **387**, 176.

97. Guo, B., Ye, Z.Z., and Wong, K.S. (2003) *J. Cryst. Growth*, **253**, 252.

98. Soukoulis, C.M., Jiang, X.Y., Xu, J.Y., and Cao, H. (2002) *Phys. Rev. B*, **65**, 041103.

99. Huang, M.H., Mao, S., Feick, H., Yan, H.Q., Wu, Y.Y., Kind, H., Weber, E., Russo, R., and Yang, P.D. (2001) *Science*, **292**, 1897.

100. Sarko, M., Song, J.K., Blackledge, C.W., Swart, I., Leone, S.R., Li, S., and Zhao, Y. (2005) *Chem. Phys. Lett.*, **404**, 171.

101. Yamamoto, A., Kido, T., Goto, T., Chen, Y., Yao, T., and Kasuya, A. (2000) *J. Cryst. Growth*, **214**, 308.

102. Reynolds, D.C., Look, D.C., Jogai, B., Litton, C.W., Cantwell, G., and Harsch, W.C. (1999) *Phys. Rev. B*, **60**, 2340.

103. Kohan, F., Ceder, G., Morgan, D., and Van de Walle, C.G. (2000) *Phys. Rev. B*, **61**, 15019.

104. Krause-Rehberg, R. and Leipner, H.S. (1999) *Positron Annihilation in Semiconductors*, Solid-State Sciences, Vol. **127**, Springer, Berlin.

105. Koida, T., Chichibu, S.F., Uedono, A., Tsukazaki, A., Kawasaki, M., Sota, T., Segawa, Y., and Koinuma, H. (2003) *Appl. Phys. Lett.*, **82**, 532.

106. Ohnishi, T., Komiyama, D., Koida, T., Ohashi, S., Stauter, C., Koinuma, H., Ohtomo, A., Lippmaa, M., Nakagawa, N., Kawasaki, M., Kikuchi, T., and Omote, K. (2001) *Appl. Phys. Lett.*, **79**, 536.

107. Jung, S.W., Park, W.I., Cheong, H.D., Yi, G.-C., Jang, H.M., Hong, S., and Joo, T. (2002) *Appl. Phys. Lett.*, **80**, 1924.

108. Teke, A., Özgür, Ü., Doğan, S., Gu, X., Morkoç, H., Nemeth, B., Nause, J., and Everitt, H.O. (2004) *Phys. Rev. B*, **70**, 195207.